



Large Eddy Simulations of a High-Speed Low-Pressure Turbine Cascade with Purge Flow

MASTER OF AEROSPACE ENGINEERING

End of Study Internship Report
2022/2023

Author:

David W. PERKINS

Supervisor:

Florent DUCHAINE

Submission Date - September 11, 2023

Acknowledgments

I would like to thank Dr. Florent Duchaine for his valuable insight throughout this project, and for providing me with the resources needed in order to succeed. I would also like to thank him for his helpful feedback, which made this report all the better.

I would also like to thank the CERFACS teams for their welcome, in particular Jérôme Dombard, Carlos Pérez Arroyo, and Nicolas Odier who went out of their way to make me feel included at CERFACS. Their introductions to AVBP were not only useful, but essential to this project.

Thanks also to the Centre de Calcul Recherche et Technologie (CCRT) for providing me access to the supercomputer, TOPAZE, which gave me the computational power needed to study this interesting case.

Thanks to the ISAE-SUPAERO teaching department for giving me the technical background to thrive during this internship. I appreciated greatly the experience at ISAE-SUPAERO and the invaluable perspective it has given me on life.

Of course, a big thanks to all of my friends in Toulouse who laughed along with me and gave me a push in the right direction when I needed one.

Finally, a thank you to my family for letting me go on the adventure of a lifetime and always supported me, even from thousands of miles away.

SUMMARY:

Future turbofan designs are expected to include gearboxes to allow for the decoupling of the fan and the low-pressure turbine. Doing so will increase efficiency, but change the design point for low-pressure turbines from a relatively low rotation speed to high-speed. To study these new high-speed low-pressure turbines, the experimental SPLEEN linear turbine cascade is studied using Large Eddy simulation (LES). Using LES, these simulations capture engine-relevant turbulence, transition, and high Mach number physics that are expected in this operating regime. These simulations are extended to include the technological effect of a blade-rotor cavity, and a sealing purge flow between these two components. The losses in the cascade are analyzed and compared to experiment, showing good predictive capabilities of LES.

KEYWORDS: Turbine, Large Eddy Simulation, Cavity, Purge Flow, Losses

Contents

1	Introduction	1
2	Work Context	2
3	Modeling and Numerics in AVBP	3
3.1	Fundamental Equations	3
3.1.1	LES Closure in AVBP	3
3.1.2	Turbulence	5
3.1.3	LES Filtering	7
3.2	Meshing	8
3.3	Numerics	8
3.3.1	Boundary Conditions	8
3.3.2	Convective Schemes	9
3.3.3	Diffusive Scheme	9
3.3.4	Time Stepping Method	9
3.3.5	Artificial Viscosity	10
3.4	Post Treatment	10
4	Modeling the SPLEEN Low-Pressure Turbine Cascade	11
4.1	A Description of the SPLEEN Turbine Cascade	12
4.2	Numerical Methods	13
4.2.1	Meshes Used	15
4.2.2	Turbulence Injection	18
4.2.3	Inlet Angle Determination	20
4.3	Results	22
4.3.1	Validation of LES Results	24
4.3.2	Investigation of Instantaneous Flow Fields	27
4.3.3	Characterization of Time-Averaged Flow Fields	29
4.3.4	Cavity Effects on Time-Averaged Flow	34
4.3.5	Comparison of Plane 06 Downstream of Blades	36
4.3.6	Comparison to Experimental Data	39
4.3.7	Categorization of Turbulent Structures	40
4.4	Discussion	44
5	Conclusion	45
6	Perspectives	46
A	Turbulent Injection Methods, Detailed	47
A.1	Kraichnan’s Method	47
A.2	Bailly’s Method	48
B	Bug Correction for Turbulent Injection Methods	52

List of Figures

1	HIT turbulent kinetic energy spectrum [5]	5
2	VKI wind tunnel schematic[45].	12
3	Wind tunnel test section cross section[45].	12
4	Geometry with cavity, periodic right wall hidden.	14
5	Cavity geometry with removed portion in red.	15
6	Overall mesh comparison.	16
7	A crinkle-slice view of one of the blades at $z/H = 0.5$, Mesh P.	17
8	A crinkle-slice focused on one of the blades at $z/H = 0.5$, Mesh P, zoomed out.	17
9	Cavity mesh comparison.	18
10	Instantaneous inlet angle distribution.	20
11	Instantaneous Plane 02 angle distribution using initial inlet angle.	20
12	Instantaneous u velocity distribution in centerline of computational domain, y -plane view.	21
13	Instantaneous angle progression in xz midplane with contours of w velocity.	21
14	Secondary flow identification in the blade to blade passage region [56].	23
15	Plane 02 angle distribution, no cavity, LW.	25
16	Plane 02 angle distribution, no cavity, TTGC.	25
17	Turbulence intensity evolution, no cavity, LW.	26
18	Turbulent integral length scale evolution, no cavity, LW.	26
19	Isentropic Mach profile at $z/H = 0.3$, no cavity, LW.	26
20	Isentropic Mach profile at $z/H = 0.5$, no cavity, LW.	26
21	Isentropic Mach profile at $z/H = 0.3$, no cavity, TTGC.	27
22	Isentropic Mach profile at $z/H = 0.5$, no cavity, TTGC.	27
23	Instantaneous velocity magnitude field, no cavity.	28
24	Instantaneous velocity magnitude field, cavity without purge flow.	28
25	Instantaneous velocity magnitude field, cavity with purge flow.	29
26	Q -criterion isosurface, $Q = 5E7 \text{ s}^{-2}$, no cavity.	29
27	Q -criterion isosurface, $Q = 5E7 \text{ s}^{-2}$, cavity no purge flow.	30
28	Q -criterion isosurface, $Q = 5E7 \text{ s}^{-2}$, cavity with purge flow.	30
29	Q -criterion isosurface, $Q = 5E7 \text{ s}^{-2}$, colored by vorticity, view upstream, no cavity.	32
30	Blade skin friction comparison, negative x/S is the pressure side.	33
31	Comparison of isentropic Mach number profiles.	33
32	Cavity streakline perturbation.	34
33	Cavity streakline perturbation, view down cavity.	34
34	Vortical structures comparison, Q -criterion isosurface at $Q = 5E7$, colored by vorticity in x direction.	35
35	TKE development in blade passage.	36
36	Plane 06 pressure loss coefficient plots.	37
37	Plane 06 vorticity with secondary velocity directions.	38
38	Plane 06 TKE with ξ contours.	38
39	Plane 06 energy loss coefficient comparison to experimental results.	39
40	Plane 06 pitchwise averaged deviation from ideal turning angle.	40
41	Plane 06 pitchwise averaged ξ .	40
42	Diagram of the Lumley triangle and turbulence triangle non-linear anisotropy invariant maps. The limiting states of componentiality are label along with the plane-strain limit (dashed line) for reference [60].	41
43	Barycentric anisotropic turbulence triangle colormap.	42

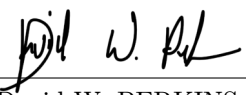
44	xy plane at $z/H = 0.3$ turbulence anisotropy.	43
45	Turbulent anisotropy downstream evolution with ξ contours.	44
46	Local frame $(\tilde{k}_1, \tilde{k}_2, \tilde{k}_3)$ in \mathbf{k} space corresponding to $(e_\theta, e_\varphi, e_r)$ in spherical coordinates, and representation of the Fourier component $\hat{\mathbf{u}}(\mathbf{k}) = \hat{\mathbf{u}}_a - i\hat{\mathbf{u}}_b$ [63].	49

DECLARATION OF AUTHENTICITY

This assignment is entirely my own work. Quotations from literature are properly indicated with appropriated references in the text. All literature used in this piece of work is indicated in the bibliography placed at the end. I confirm that no sources have been used other than those stated.

I understand that plagiarism (copy without mentioning the reference) is a serious examinations offence that may result in disciplinary action being taken.

September 11, 2023
Date


David W. PERKINS

1 Introduction

The focus of the present work is the study of secondary and leakage flow effects in high-speed low-pressure turbines (LPT), as described by the SPLEEN project¹. This EU project focuses on developing knowledge and tools to design such a next-gen turbine by instrumenting a cascade at engine-realistic conditions. These high-speed low-pressure turbines are a key technology for the engineering of Ultra High Bypass Ratio (UHBR) turbofans, whose development is driven by environmental and economic requirements. A high bypass ratio engine will have increased fan diameter, which must have a reduced fan rotation speed in order to reduce tip losses. This reduction in fan rotation speed is typically accomplished via a gearbox between the fan rotor and the intermediate pressure compressor (IPC) [1]. As the IPC and the LPT are mechanically linked, this allows the LPT to rotate at a higher rate, which allows for both the fan and the low-pressure turbine to operate at more optimal speeds, which improves overall cycle efficiency relative to a traditional turbofan [2].

Consequently, these engine designs require that the LPT operate at transonic exit Mach numbers ($M_{out} > 0.9$) and low-Reynolds numbers [3]. In general, numerical simulation tools are becoming increasingly complex in order to provide insight into turbomachinery flows. Despite this, the conditions in high-speed LPTs remain difficult to simulate as there can be developed shocks, laminar to turbulent boundary layer transition, and rotor-stator interaction between moving parts. High levels of turbulence as well as unsteadiness necessitate the use of Large Eddy Simulations (LES) which are significantly more expensive than traditional Reynolds Averaged Navier-Stokes (RANS) simulations or unsteady RANS (URANS) simulations.

To better understand the flow physics present in these high-speed low-pressure turbines, this work simulates experimental flows using LES via the AVBP code from CERFACS. LES has a few advantages over RANS or URANS in this context. The main advantage is that LES explicitly resolves a large portion of turbulent fluctuations, which reduces the need for turbulence models (such as the $k - \epsilon$ model for RANS). Instead, LES uses a subgrid-scale (SGS) model to represent small scales of turbulence that cannot be resolved by the mesh. By directly solving a large part of the turbulent spectrum, LES can capture flow physics that otherwise may be difficult to model, including boundary layer transition, large separation, and acoustics. In the case of the SPLEEN experimental cascade, data has been collected [4] to quantify the turbulent statistics actually present in order to reproduce their effects in a simulation. Additionally, the measurement of these quantities allows for a broader understanding of flow physics and their dependency to variations in operating conditions.

The experimental SPLEEN cascade is a variable set up that recreates the effects in a real high-speed low-pressure turbine complete with rotating rods and a cavity. The rotating rods mimic the behavior of passing wakes from an upstream stage, and the cavity allows for purge flow to be injected into the cascade from a realistic geometry. The complexity of the experiments is increased throughout the testing campaign, starting with experiments performed without the wake generators or the cavity, then adding the wake generators, then finally adding the cavity. Simulating the entire experimental set up is prohibitively expensive due to the computational cost, and consequently the main challenge in this project is to create a robust, affordable simulation. This simulation should also capture the effects of the purge flow cavity and the purge flow's effects on the main flow as it relates to the observed blade profiles, without including the rotating bars.

In the following section, the company and its organization is presented. The bulk of this report is in Section 4, which covers some of the scientific theory surrounding LES of LPTs, the key methods, the main work performed, as well as the results and their discussion. Finally, some

¹<https://www.h2020-spleen.eu/>

overall conclusions on the internship are presented in Section 5.

2 Work Context

This internship was performed at le Centre Européen de Recherche et de Formation Avancée en Calcul Scientifique (CERFACS), located in southwest Toulouse. CERFACS is a privately owned research center, focusing on modeling and simulation. This basic and applied research center was created in 1987 by eleven members: Aérospatiale, CNES, CNRS, INPT, Inria, Insa, Matra-Marconi Space, Météo-France, Onera, and Midi-Pyrénées. Currently, many CERFACS projects are multinational and/or interdisciplinary and are often strongly coordinated with one of its seven shareholders: Airbus Group, Cnes, EDF, Météo France, Onera, Safran and Total. Other key relations include CNRS, Irit, CEA, and Inria. These collaborations allow CERFACS to deal with major scientific and technical research problems of societal and industrial interest.

At CERFACS, there are a number of interns as well as young PhD students who are supported by a team of experienced professionals in a variety of fields, ranging from algorithm development, to computational fluid dynamics, to climate modeling. Each of these teams are backed by a number of information technology personnel, human resources staff, and janitorial staff. The wide variety of teams also employs a wide variety of backgrounds, including (but not limited to) physicians, applied mathematicians, numerical analysts, and software engineers.

The stated objectives of CERFACS are to:

- Develop scientific and technical researches in order to improve advanced computing methods, including a better consideration of the related physical processes as well as the development of performing algorithms for the new computers' architectures,
- Allow either solely or shared access to computers with new architecture, being able to gain performances,
- Transfer this scientific knowledge and technical methods for application to big industrial sectors,
- Train high qualified people and offer an advanced training for the fields and selected application themes.

There are four main teams at CERFACS:

- **Climate modeling and Global Change (GLOBEC):** which conducts fundamental and applied research for climate modeling, developing advanced models to couple the oceans, the atmosphere, and other components of the climate system. These systems are increasingly complex, requiring the use of high performance computing (HPC) to accurately reproduce the dynamics of the observed climate. This team's main goals are to develop high level softwares for modeling the complex links in climate science, and to improve models on climate variability and predictability using HPCs.
- **Computational Fluid Dynamics (CFD):** which focuses on flow simulation and develops advanced models applicable to planes, rockets, engines, turbines, and many others. This team develops key tools for applied aerodynamic fields and is intricately linked to HPC, as the efficiency and reliability of CFD simulations is of primary interest.
- **Parallel Algorithms & sScientific sOftware Operational Perfomances (ALGO-COOP):** which works on numerical algorithms, large scale computing, software engineering, adaptive mesh generation, parallel load balancing, and others. This team is responsible

for many of the tools that are incredibly useful for supporting the other research teams. The ALGO-COOP team is also involved in the increasingly important fields of machine learning and artificial intelligence.

- **IT management and user support:** which manages standard computing frames necessary for the operation of CERFACS (such as internet, mail, accounting systems, etc.) but also the in-house High Performance Computing systems necessary for simulations. This team also manages the connection between CERFACS to other national (Genci) and international (Prace and Incite) computing resources for research purposes.

3 Modeling and Numerics in AVBP

As outlined in the introduction, the CFD program used at CERFACS is the LES solver AVBP, developed by CERFACS. The following section will detail the fundamental equations and numerics used by AVBP in the context of a non-reacting, turbulent flow typically seen in turbo-machines.

3.1 Fundamental Equations

As a CFD software, AVBP finds numerical solutions to the Navier-Stokes equations. This well-known set of equations has been studied extensively since the 19th century. Initial solutions to these equations were constructed with very strong simplifying assumptions, however modern problems require more relevant hypotheses, which in turn requires increased complexity in the equations. Thanks to the exponential growth in computational sciences, the Navier-Stokes equations have become more approachable with fewer assumptions.

The previously mentioned Navier-Stokes equations are:

$$\frac{\partial \rho}{\partial t} + \frac{\partial \rho u_i}{\partial x_i} = 0 \tag{1}$$

$$\frac{\partial}{\partial t} \rho u_i + \frac{\partial}{\partial x_j} (\rho u_i u_j + p \delta_{ij} - \tau_{ij}) = \rho F_i; \quad i = 1, 2, 3 \tag{2}$$

$$\frac{\partial \rho E}{\partial t} + \frac{\partial}{\partial x_j} (\rho E u_j + p \delta_{ij} u_j - u_i \tau_{ij} + q_j) = \rho F_j u_j + \dot{Q} \tag{3}$$

where ρ is the density of the fluid, u is the velocity vector, E is the total Energy, τ_{ij} is the viscous stress tensor, p is the pressure, q is the heat flux, \dot{Q} is the heat source term, and F is the external force applied. Here, δ_{ij} is the classically defined Kronecker delta function, and the repeated subscripts use Einstein notation to indicate summation.

These five equations are continuity equations, where the first equation is the conservation of mass, the second through fourth form the conservation of momentum, and the last is the conservation of energy. These equations constitute a set of partial differential equations (PDEs) which are known to be strongly dependent on two additional sets of information, the boundary conditions and the initial condition. A quick examination of these five equations reveals eight unknowns, and so the problem is not closed.

3.1.1 LES Closure in AVBP

These closure variables, p , the pressure, τ_{ij} , the viscous stress tensor, μ , the dynamic viscosity, and q , the heat flux must be determined. For the simulations discussed in this report, these are closed with the following state and behavior laws.

For the state law, it is assumed that the fluid is a calorically perfect gas, giving

$$p = \rho r T, \quad (4)$$

where r is the gas constant of the local mixture seen in the flow at a given instant. For this flow,

$$r = \frac{\mathcal{R}}{W} \quad (5)$$

where \mathcal{R} is the universal gas constant, $\mathcal{R} = 8.3145 \text{ kg.m}^2.\text{s}^{-2}.\text{K}^{-1}.\text{mol}^{-1}$. For this simulation, the fluid (air) is simplified as a single species with molecular weight $W_{air} = 0.02885 \text{ kg.mol}^{-1}$. Since the air is assumed to be calorically perfect, the constant pressure c_p and constant volume c_v specific heat capacities are constant, and their ratio $\gamma = c_p/c_v$ is known as the adiabatic exponent. For air under this assumption, the internal energy, e , the enthalpy, h , and the heat capacity depend only on the temperature. The total energy of the air can be expressed as

$$E = \frac{rT}{\gamma - 1} + \frac{1}{2}\rho|\mathbf{u}|^2, \quad (6)$$

which closes the pressure, p .

To determine the viscous stress tensor, the Newtonian fluid hypothesis is used in combination with the Stokes hypothesis to relate the bulk viscosity and the dynamic viscosity. Together, these two assumptions give that the viscous stress tensor as:

$$\tau_{ij} = \mu \left(\frac{\partial u_j}{\partial x_i} + \frac{\partial u_i}{\partial x_j} \right) - \frac{2}{3}\mu \left(\frac{\partial u_i}{\partial x_i} \right), \quad (7)$$

which also exposes the closure variable, μ , the dynamic viscosity. For the dynamic viscosity, Sutherland's law is used, which allows for the straightforward computation of the dynamic viscosity as a function of temperature. For the air used in the simulation, this equation is

$$\mu(T) = \mu_{ref} \left(\frac{T}{T_{ref}} \right)^{\frac{3}{2}} \frac{T_{ref} + S}{T + S} \quad (8)$$

with reference values $\mu_{ref} = 1.807\text{E} - 5 \text{ kg.m}^2.\text{s}^{-1}$ and $T_{ref} = 273.15 \text{ K}$. The parameter S is the Sutherland constant, here $S = 110.6 \text{ K}$ for the simulated air mixture.

The last missing piece, the heat flux, q , is modeled via a conduction process using Fourier's law as:

$$q_i = -\lambda \frac{\partial T}{\partial x_i}, \quad (9)$$

where λ is the thermal conductivity. In this simulation, the thermal conductivity is determined by the Prandtl number of air, which is assumed to be constant in time in space with a value $Pr = 0.71$.

$$\lambda = \frac{\mu c_p}{Pr} \quad (10)$$

With these assumptions, all four of the closure variables can be determined and the NS equations are closed.

3.1.2 Turbulence

A key observation is that the NS equations are inherently non-linear, and this non-linearity is understood to be the underlying source for the development of turbulence. Turbulence, while difficult to define, is best described as a three dimensional time-dependent motion driven by vortices causing velocity fluctuations to spread across many wavelengths in a chaotic (random) manner. A turbulent flow is often modeled as a stochastic process, where the velocity vector, \mathbf{u} , can be decomposed into a mean quantity, $\bar{\mathbf{u}}$, and a fluctuating part, $\mathbf{u}'(t)$:

$$\mathbf{u}(t) = \bar{\mathbf{u}} + \mathbf{u}'(t) \quad (11)$$

Turbulence is typically studied and understood through its simplest case, homogeneous isotropic turbulence (HIT). The addition of these two properties, homogeneity and isotropy, allow for a clear mathematical description of the problem. Briefly, homogeneity means that the properties of the fluctuations (the turbulence) are invariant with translation. Isotropy means that the fluctuations are invariant with rotation.

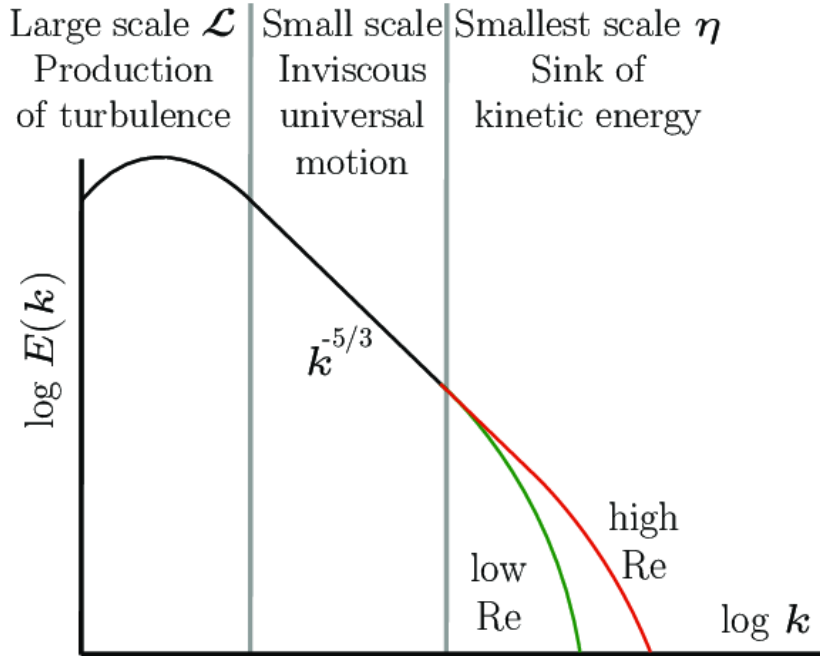


Figure 1: HIT turbulent kinetic energy spectrum [5]

A classical diagram (Figure 1) for explaining HIT is the the turbulent kinetic energy spectrum. The above figure shows the turbulent kinetic energy as a function of the wavenumber (k) of the turbulent scale. The turbulent kinetic energy (TKE) can be defined as:

$$TKE = \frac{3}{2} u'_{rms}{}^2, \quad (12)$$

where u'_{rms} is the root-mean-square of the turbulent velocity fluctuations. This energy cascade is well studied and is typically described by a process where the mean flow produces energy that is transferred to the inertial scales via large tubular vortices. In Figure 1, the

variable k is the wavenumber of the turbulent structure, equal to the inverse of the length of the structure. Thus, a large k is related to very small structures, and a small k is linked to large structures in the mean flow. These large structures interact and their stretching generates smaller scale tubular vortices. These increasingly smaller vortices continue to interact, cascading energy from the large scales to very small scales. At these very small scales, the energy is finally dissipated via molecular viscosity [6]. These very small scales are classically defined by the Kolmogorov length, η_K ,

$$\eta_K = \left(\frac{\nu^3}{\varepsilon} \right)^{1/4}, \quad (13)$$

where ε is the average rate of dissipation of turbulent kinetic energy per unit mass, and ν is the kinematic viscosity of the fluid. This is the only combination of these two variables that gives a length, as ε has dimensions $(\text{length})^2/(\text{time})^3$, and ν has dimensions $(\text{length})^2/(\text{time})$.

Figure 1 highlights the disparity in energy content between the different scales in the turbulent flow. In general, the larger scales contain a majority of the energy, while the dissipative scales contain only a small portion. This is a key part of the LES model: LES resolves many scales of turbulence which accurately describes the energetic scales critical for the behavior of the flow, and models the small dissipative portion. Moreover, these small dissipative scales are considered to be more universal [7] and therefore less dependent on the geometry simulated, which makes modeling them more generally applicable. This is in contrast to URANS, which does not resolve any turbulent scales, and DNS, which must resolve all turbulent scales down to the very small dissipative scale.

One important issue with HIT is that it clearly is not representative of flows seen in most industrial contexts. For instance, the flow near any wall is perturbed near it and so it becomes neither homogeneous nor isotropic, and consequently, the flow through a complex feature such as a linear turbine cascade is not either.

There are a few key quantities for describing turbulence. The first of these is the turbulence intensity,

$$TI = \frac{u'_{rms}}{|\bar{\mathbf{u}}|}, \quad (14)$$

where u'_{rms} is the root-mean-square of the turbulent velocity fluctuations and $|\bar{\mathbf{u}}|$ is the magnitude of the mean velocity vector. This can be computed as

$$u'_{rms} = \sqrt{\frac{1}{3} ((u'_x)^2 + (u'_y)^2 + (u'_z)^2)} \quad (15)$$

or

$$u'_{rms} = \sqrt{\frac{1}{3} \left((\overline{u_x^2} - \bar{u}_x^2) + (\overline{u_y^2} - \bar{u}_y^2) + (\overline{u_z^2} - \bar{u}_z^2) \right)}, \quad (16)$$

where $\overline{u_i^2}$ is the average of the squared i th velocity component, and \bar{u}_i^2 is the square of the average i th velocity component. Here, $|\bar{\mathbf{u}}|$ is the magnitude of the mean velocity vector.

Another key quantity for describing turbulence is the integral length. This length represents the average size of vortices containing the highest energy. Roach [8] proposes that the integral length scale (Λ) can be computed via extrapolating the power spectrum of the velocity functions ($E(f)$) as the frequency approaches zero by

$$\Lambda = \left[\frac{E(f)|\bar{\mathbf{u}}|}{4|\bar{\mathbf{u}}|^2} \right]. \quad (17)$$

This value can also be estimated via the auto-correlation of the velocity field at two different positions (x_1, x_2) at the same time [9] as

$$\Lambda = |\bar{\mathbf{u}}| \int_0^\infty \frac{u'_x(x_1, t)u'_x(x_2, t)}{\sqrt{u_x'^2(x_1, t)}\sqrt{u_x'^2(x_2, t)}} dt. \quad (18)$$

3.1.3 LES Filtering

In the context of LES, the scales that are resolved are dependent on both the mesh and on the filter size. Selecting the filter size, Δ , is not trivial, but it is ideally chosen such that approximately 80% of the turbulent kinetic energy (TKE) is resolved. This criterion is also known as the Pope criterion [10].

With this filter size defined, the LES formalism for a given quantity, ϕ , can be decomposed into a resolved part $\langle \phi \rangle_\Delta$ and a modeled part, ϕ' as

$$\phi = \langle \phi \rangle_\Delta + \phi' \quad (19)$$

where the filtering process is defined based on Leonard [11] and can be understood as

$$\langle \phi(x) \rangle_\Delta = \int \phi(x')G(x, x'; \Delta)dx', \quad (20)$$

where G is the filter function dependent on the filter width, Δ . When the filtering follows a Favre operation (averaged weighted according to the density), then

$$\phi = \bar{\phi} + \phi'' \quad (21)$$

where the Favre operation is

$$\bar{\phi} = \frac{\langle \rho \phi \rangle_\Delta}{\langle \rho \rangle_\Delta}. \quad (22)$$

Applying this filter to the original NS equations gives the filtered LES equations as (where the subscript Δ is omitted on the filtering operator for clarity):

$$\frac{\partial \bar{p}}{\partial t} + \frac{\partial \bar{p} \langle u_i \rangle}{\partial x_i} = 0, \quad (23)$$

$$\frac{\partial}{\partial t} \bar{\rho} \langle u_i \rangle + \frac{\partial}{\partial x_j} (\bar{\rho} \langle u_i \rangle \langle u_j \rangle + \bar{p} \delta_{ij} - \bar{\tau}_{ij} - \tau_{ij}^{SGS}) = \bar{\rho} F_i; \quad i = 1, 2, 3, \quad (24)$$

$$\frac{\partial \bar{\rho} \langle E \rangle}{\partial t} + \frac{\partial}{\partial x_j} (\bar{\rho} \langle E \rangle \langle u_j \rangle + \bar{p} \delta_{ij} \langle u_j \rangle - \langle u_i \rangle \langle \tau_{ij} \rangle - \langle u_i \rangle \tau_{ij}^{SGS} + \bar{q}_j + q_j^{SGS}) = \bar{\rho} F_j \langle u_j \rangle + \dot{Q}. \quad (25)$$

The above equations introduce the subgrid scale stress tensor, τ_{ij}^{SGS} , and the subgrid scale heat flux, q_j^{SGS} . These two subgrid quantities are used to model the effects of the vortices below the mesh resolution. In AVBP, there are several options for these models: Smagorinsky [12], Filtered Smagorinsky, Dynamic Smagorinsky [13], WALE [14], SIGMA [15], and the k-equation.

3.2 Meshing

The previously mentioned equations are continuous, however the solution of these equations via computer require discretization in both time and space. The spatial discretization of the problem is driven by the mesh. For LES computations, it is well known that the spatial resolution has a direct impact on the quality of the results [16][17]. This is often due the practical link of the mesh size to the spatial filtering in the LES method.

AVBP uses unstructured meshes. Unstructured meshes are easier to generate and manipulate for complex geometries (such as those required for turbomachinery) as compared to structured meshes. Another advantage is that these unstructured meshes allow for the incorporation of different types of cells, such as prism layers to better capture gradients in the boundary layer. Unfortunately, unstructured meshes require more memory to store a more complicated connectivity matrix, and the algorithmic development for these methods is more complex.

Furthermore, AVBP uses a cell-vertex approach to store the information computed on the mesh. This is a residual method that stores information at the mesh nodes, and the equations are solved using the primary control volumes as indicated by the mesh. One advantage of this method is that a complex geometry will necessarily have more cells than vertices, which means that storing the information at these vertices will result in a lower memory cost than defining the cell centers and storing the information there. Additionally, this method is more robust to distorted meshes [18].

3.3 Numerics

With the spatial discretization of the problem determined via the mesh, this discretized domain must be related to the continuous equations as mentioned before. The numerical schemes implemented to discretize the equations also known to strongly influence the quality of the results. This follows from the fact that the numerical schemes influence the diffusion and dispersion of information in the domain and so selecting a nondiffusive and nondispersive scheme gives more accurate results. More information on the numerical methods in AVBP can be found in Schönfeld, 1999 [19].

3.3.1 Boundary Conditions

The selection of boundary conditions for PDEs is a crucial problem that strongly influences the physics and the solution. One additional difficulty with boundary conditions applied to the compressible Navier-Stokes equations is that there are waves (acoustic, entropy, and convective) hidden within these equations propagating at varying speeds into and out of the domain.

Within the fluid domain, the handling of these waves is straightforward, as at a given point in the domain there is the required information nearby to allow for these waves to propagate correctly. Near the boundaries, however, waves should be traveling out of the domain of information, and correspondingly there should be additional waves entering the domain. These waves entering the domain are not trivial to determine.

An excellent approach to determine these waves is the use of Navier-Stokes Characteristic Boundary Conditions (NSCBCs) [20]. First introduced by Poinot and Lele in 1992, this method works by rewriting the NS equations in terms of characteristic equations, giving the corresponding characteristic wave equations. With this formulation, the imposed physical quantities (e.g., at an inlet), together with the known waves (e.g., waves going out the inlet), can be used to determine the unknown waves (e.g. waves coming in the inlet) with sufficient accuracy. This formulation allows for the careful treatment of the boundary conditions, preventing the "trapping" of waves and reducing nonphysical reflections at the boundaries. Further developments to this method

allow for the introduction of turbulence at inlets [21], more robust treatment of the boundary transverse quantities, and the "soft" imposition of total pressure and total temperature.

For the following simulations, the main inlet imposes a uniform total pressure and total temperature, using the NSCBC method described by Odier et al [22], which uses a locally one-dimensional inviscid assumption over the boundary to solve for the ingoing/outgoing waves over the boundary. This inlet also allows for the imposition of incoming turbulence, described in Section 4.2.2 and fully detailed in Appendix A. For cases where there is a cavity, the inlet of the cavity is an NSCBC with an imposed normal mass flow rate at a set static temperature. The outlet of the simulated domain is also an NSCBC with an imposed static pressure, with additional treatment of transverse wave terms [23]. All of the walls in the simulated domain (except for the shroud wall, which is treated as an adiabatic slip wall) are considered to be adiabatic, no slip walls. These walls all use the wall-adapting local eddy-viscosity (WALE) model [14] to model the subgrid stress tensor.

3.3.2 Convective Schemes

In AVBP, the code provides several options for the convective scheme: the finite volume Lax-Wendroff (LW) scheme (second order in space and time) [24], as well as some finite element schemes, TTGC (third order in space and time) and TTG4A (third order in space, fourth order in time) which are based on two-step Taylor Galerkin methods [25]. Other options in AVBP are proposed but are not discussed here.

On the same mesh, a higher order scheme should provide a better result. The tradeoff for this is that the higher order schemes also have increased computational cost. In the case of AVBP, the higher order TTGC and TTG4A schemes are nearly 2.5 times more expensive than the LW scheme, but give better results on academic configurations (e.g. convection of a vortex). The LW scheme tends to give sufficient accuracy for purely aerodynamic problems [26], and will be used primarily throughout this work.

3.3.3 Diffusive Scheme

The diffusive scheme offered by AVBP is the finite element 2Δ scheme developed by O. Colin [27].

3.3.4 Time Stepping Method

As for the temporal discretization of the problem, AVBP uses explicit schemes with a time step derived either from the CFL number or the Fourier number, whichever gives the smaller time step, based on the whole computational domain.

The CFL number is driven by the stability constraint for convection schemes, where the user must give AVBP an operating CFL number, c , such that $c \leq c_c$, where c_c is the critical CFL number to ensure L^2 stability. In a turbomachinery flow, this is the main constraint on the timestepping. In AVBP, the CFL number gives cell's timestep proportional to:

$$\Delta t_{CFL} \propto |C| \tag{26}$$

with $|C|$ as the cell surface or volume (directly driven by the size of the mesh). AVBP then selects the minimum over all cells as the timestep required by the CFL condition. In turbomachinery flows this can be extremely small, as the cell size required to properly resolve a boundary layer or intricate geometric features tends to be very small.

The Fourier number is much like the CFL number but for diffusive terms. In AVBP, the user selects an operating Fourier number, d less than the critical, d_c for stability. This imposes a timestep on the cell proportional to:

$$\Delta t_d \propto \frac{|C|^2}{D}, \quad (27)$$

where D is a diffusion coefficient. In a nonreactive turbomachinery flow, diffusion coefficients tend to be quite small, and so the timestep imposed by the Fourier number is on the same order of magnitude as that imposed by the CFL number.

3.3.5 Artificial Viscosity

Despite their high order accuracy, these convective and diffusive models need additional artificial viscous damping to stabilize the solution and smooth the distribution process as the information in a given cell is transferred back to its nodes [28] [19]. Without artificial viscosity, spurious modes can appear in the solution. One of these modes is described as a checkerboard mode, which are nonphysical oscillations [29] that appear due to the centered numerical method combined with the collocation of the variables [30]. In AVBP, some wiggles (spurious waves) often appear due to the slightly dispersive nature of the convective schemes.

In AVBP, these numerical issues are typically dealt with via artificial viscosity, applied as second-order and/or fourth-order diffusion. These additional diffusion terms are generally triggered by a sensor in AVBP, including a honey "sensor" (applies the artificial viscosity uniformly over the whole domain), the Jameson sensor (applies based on pressure gradients), and the Colin sensor (applies based on total energy and species densities). For LES turbomachinery flows, the Jameson sensor is typically appropriate, and will be used throughout this work.

3.4 Post Treatment

In the case of experiments, there is a limited amount of data that can be collected easily. One of the greatest advantages to simulations is that they provide a wealth of data over the whole domain. This data requires post treatment temporally and spatially in order to reduce the information and draw conclusions. Typically, this reduction of information is done via averaging, either in time or in space. This allows for the extraction of key features in crossflow planes, or the recovery of averaged quantities over key planes, such as the evolution of total pressure from inlet to outlet. This reduction of information is necessary to reduce complexity and describe the key physics.

Averaging is typically taken as a simple process. However, in the context of CFD, and more specifically turbomachinery, there is a method for averaging which is correct in the sense that it conserves key variables of interest [31]. For variables that are governed by conservative equations in the underlying solver, it is best to continue to conserve these with the averaging procedure, such that the averaged field is also conservative. In this way, the mass flow weighted average is easily defined, where the $\langle \cdot \rangle$ operator denotes either spatial or temporal averaging:

$$\phi^{avg} = \frac{\langle \rho U_i \phi \rangle}{\langle \rho U_i \rangle}. \quad (28)$$

In cases where the CFD results are to be compared with experimental ones, the averaging processes should be the same. Typically, CFD for turbomachinery can sample the flow at the same or greater rate as the one seen experimentally. On the other hand, an experiment often provides results that are averaged over seconds, which is generally infeasible to reproduce in CFD. Instead, CFD must produce results that are statistically converged. Statistical convergence in the case of turbulent flows can be described by the convergence of statistical moments, such as the variance of the pressure fluctuations at a given point reaching a constant value after a

given sampling time. Reaching statistical convergence is often costly, as this takes additional flow through times after the flow has reached an average solution.

4 Modeling the SPLEEN Low-Pressure Turbine Cascade

As stated in the introduction, this work focuses on the secondary and leakage flow effects in high-speed LPTs, a developing area of turbomachinery research. Such a high-speed LPT is not currently in use, but this design is increasingly studied as the bypass ratio of turbofan engines continues to increase in order to reduce fuel consumption and noise [32]. As the efficiency of engines continues to increase, the combustion chamber exit temperature also tends to increase. This means that the downstream turbines see hot mainstream gas, which can potentially damage these components. To prevent this damage, cooling films are released through small holes in the turbine blades and walls, and purge flow is injected through cavities in the hub of axial turbines to prevent this hot air from entering the interstage gaps [33]. These purge flows are not only required for the functioning of the engine, but also represent up to 20% of the main compressor flow used to cool components [34]. The effects of purge flows on the efficiency of gas turbines is relevant because as engine pressure ratios and bypass ratios increase, the penalties for cooling airflows increase [35]. Overall, a better understanding of these secondary and leakage flows is needed to better optimize future high-speed LPTs.

The main difficulties in simulating flows in high-speed LPTs are: inherent unsteadiness, boundary layer transition, turbulence, and shock waves. The first difficulty greatly reduces the effectiveness of RANS, and requires URANS or LES as a starting point. Secondly, boundary layer transition is still not completely understood, and is even more difficult to simulate accurately in complex flows. High levels of turbulence make LES difficult, as the determination and injection of engine-relevant turbulence is not trivial. Lastly, shock physics often pose numerical stability problems and can require very small grid sizes to be captured accurately, or they necessitate increased artificial viscosity to obtain a solution. With the addition of technological effects (such as cavity purge flows), the corresponding grid sizes are often quite small, further increasing the cost of these simulations. These purge flows have a characteristic time that is typically much longer than the core flow through time, which also increases the cost of simulation.

Current approaches for modeling turbines use URANS or LES [36] [17] [16] [37] in order to capture unsteady phenomenon in the flow. This unsteadiness is especially crucial in the study of the effects of purge flow. Denton [38] intuitively explains that the addition of purge flows contributes to mixing, which is closely linked to entropy creation and losses in a turbomachine. More recently, these flows have been shown to modify the horseshoe vortex formation, as shown by Gallier et al [39], and more recent studies [37] [40] have shown more directly that the secondary flows at the hub are fed by the purge flow, leading to additional friction and more entropy production.

Turbulence is important in turbomachinery simulations, as it effects the movement of vortices, boundary layer transition, and the attachment (or detachment) of flow around the blades [41]. Afshar et al. [42] very recently performed an isotropy turbulence analysis for a linear LPT cascade and showed LES predicts correct turbulence transition and captures strongly anisotropic turbulent characteristics. In contrast, URANS is unable to capture these anisotropy phenomenon which reduces prediction accuracy, especially in turbomachinery flows where there is often separation and boundary layer transition. LES predictions are better in these cases because LES resolves turbulent scales to the grid size. With this increased resolution, additional care must be taken to inject realistic turbulence at the inlet of the simulated domain. Techniques for injecting this turbulence are reasonably well established, allowing for the injection of fairly realistic syn-

thetic turbulence with a lower cost [43]. These turbulence injection techniques have also been recently expanded for specific inlet types in AVBP, allowing for the generation of a characteristic inlet boundary condition where the total pressure and total temperature can be imposed [22].

This study aims to simulate such a complex high-speed LPT linear cascade and include the effects of cavity purge flows to characterize the effects of secondary flows on losses. To do so, an LES is performed to gain more insight on the experiments performed on SPLEEN linear turbine cascade, studied at the Von Karman Institute. The following section details the experimental configuration of the cascade, and section 4.2 introduces the numerical setup.

4.1 A Description of the SPLEEN Turbine Cascade

The SPLEEN turbine cascade is unique as there is experimental PIV data [44] for this high-speed, low-Reynolds, low-pressure configuration with additional characterization on the turbulence [4]. This cascade can also simulate the impacts of unsteady wakes between blade rows with moving bars as well as purge flows [45]. A thorough description of the test case can be found in the public database [46].

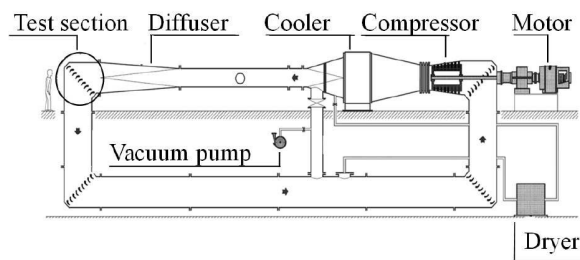


Figure 2: VKI wind tunnel schematic[45].

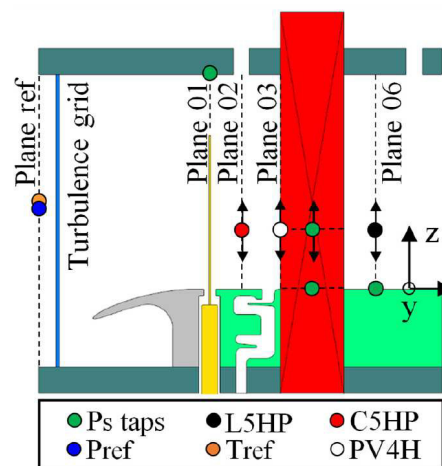


Figure 3: Wind tunnel test section cross section[45].

The Von Karman Institute (VKI) wind tunnel is shown in Figure 2. In the test section, the SPLEEN linear cascade consists of 23 blades with a span of 165 mm. Other key dimensions are: a blade chord, C , of 52.280 mm, an axial chord, C_{ax} , of 47.614 mm, and a pitch, g , of 32.950 mm. The nominal operating point is described by the outlet Mach number, $M_{out} = 0.90$ and by the outlet Reynolds number, $Re_{out} = 70000$. The freestream turbulence intensity was determined to be $\approx 2.4\%$, generated by a grid just upstream of the test section. The cascade simulates unsteady wakes with a spoked-wheel wake generator with 1.00 mm diameter cylindrical rods (yellow component in Figure 3). These diameters are reported to be similar to the trailing edge thickness of a thin LPT blade to reproduce the vortex shedding that would come from a rotor-stator combination in a real turbine. After this (optional) wake generator, there is a cavity used to inject purge/leakage flow into the test section with purge mass flow ratios ranging between 0 and 0.9% of the mean main flow.

Experimental data is collected using four types of probes: static pressure taps (Ps taps in

Figure 3), a pneumatic Cobra five-hole probe (C5HP), a pneumatic virtual four-hole cylindrical probe (PV4H), and a pneumatic L-shaped five-hole probe (L5HP). The static pressure taps at Plane 01 are used to characterize the inlet static pressure. The C5HP measures the total pressure as well as the pitch and yaw angle at Plane 02. The PV4H also measures the total pressure and pitch and yaw angle, but a fast-response version of this probe also exists to measure the unsteadiness of these conditions. Lastly, the L5HP is used to measure the outlet total pressure and pitch and yaw angle. Plane 02 (located half an axial chord upstream of the leading edge) is used to characterize the inlet flow field of total pressure and incidence on the blades. Plane 06 (located half an axial chord downstream of the trailing edge) is used to characterize the cascade losses and deviation.

4.2 Numerical Methods

In the present study, the simulation domain has two blades and applies periodic conditions in the z direction, as shown in Figure 4. This is representative of the central blades of the test section, and aims to recover the flow and potential in-row interactions between blades. Including two blades is also relevant as the sizes of turbulence seen in the experiment are fairly large relative to the blade to blade spacing (approximately one-third the pitch). Three cases are simulated: the domain with no cavity, the domain with the cavity without purge flow, and the domain with the cavity and with purge flow equal to 0.9% of the mean main mass flow.

Figure 4 colors different portions of the domain. The inlet to the domain is shown in green on the left, and the outlet is in red on the far right. The two blades are centered and colored grey. The periodic wall on the left (looking from the inlet) is colored a light blue, and the corresponding periodic wall on the right is not shown. A key feature of this domain is the blue wall, and this region below the hub wall will be referred to as the boundary layer trap. The purge flow cavity is shown in purple, and in cases without the cavity this section is removed and the light gray hub wall extends directly to the blades. The axes pictured in Figure 4 are used throughout this report.

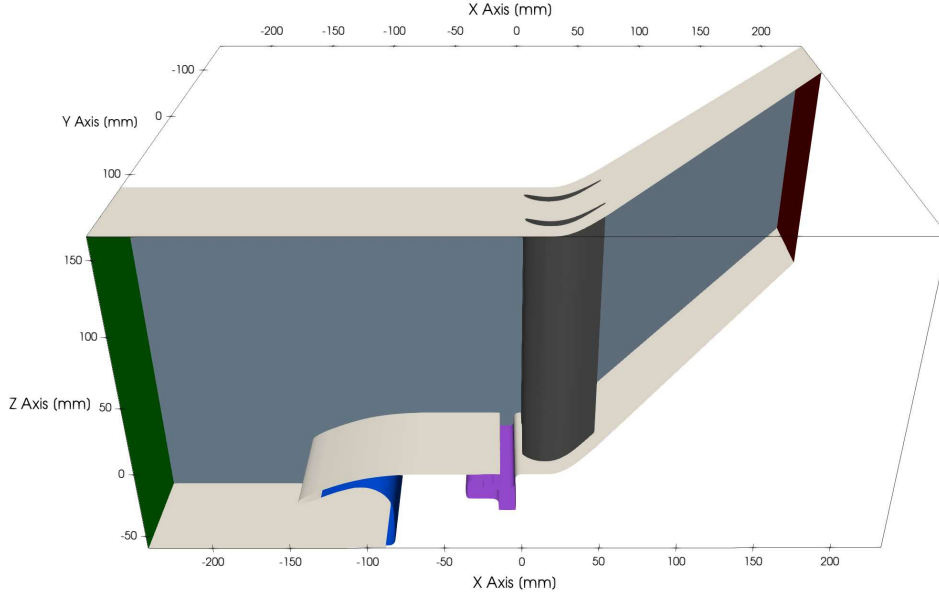


Figure 4: Geometry with cavity, periodic right wall hidden.

The inlet of the domain is 100 mm (just over $2C_{ax}$) from the leading edge of the hub tip edge, and the exit of the domain is 173 mm (in the x direction) downstream of the trailing edge of the blades. With the outlet angle of the blades at 53.8° , this corresponds to about 200 mm (over $4C_{ax}$) in the outlet flow direction until the outlet.

The Navier-Stokes equations are solved using CERFACS' Large Eddy Simulation solver, AVBP. AVBP uses a cell-vertex approach on an unstructured multielement grid. The diffusive scheme in AVBP is the finite element 2Δ scheme developed by O. Colin [27], and the convective schemes in AVBP used in this work are either the Lax-Wendroff [24] scheme or the higher order TTGC [25] scheme. For this work, additional artificial viscosity is controlled via a Jameson sensor, which applies based on pressure gradients. The sugrid-scale model used is the wall-adapting local eddy viscosity (WALE) [14], which is well suited for determining the eddy viscosity near walls and is commonly used in LES of turbomachinery. At the inlet, total pressure and total temperature are imposed according to experimental data, and the velocity direction is imposed such that the angle seen at Plane 02 is as consistent as possible to experimental data. The method for turbulence injection will be discussed in section 4.2.2, with the mathematics further discussed in Appendix A. At the outlet, a static pressure is imposed such that the isentropic Mach profile on the blades are consistent with experimental data. Both the inlet and outlet are applied using Navier-Stokes Characteristic Boundary Conditions (NSCBC) [20], even for the case of turbulence injection [22]. The hub and blade walls are considered to be adiabatic and have no slip conditions, while the shroud wall is adiabatic and a slip wall. The sides the simulated domain have periodicity conditions imposed.

The cavity geometry is provided by the SPLEEN experimental test database [46]. The complete cavity geometry provided in the database is pictured in Figure 5 below, and originally included a buffer plate before the main bend of the cavity. For simplicity, this buffer plate is removed and the cavity is shortened to focus on the physics near the main flow.

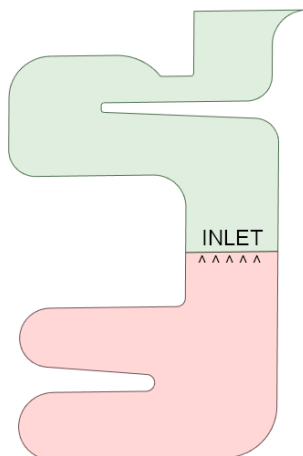


Figure 5: Cavity geometry with removed portion in red.

To implement the case without purge flow, the bottom of the reduced cavity geometry is configured in AVBP as an inlet with a target mass flow rate slightly greater than zero at a static temperature of 260K, slightly lower than the main passage flow. This allows for a nonreflective boundary condition with simple visualization based on temperature and mimics real engine purge flows which are cooler than the main passage flow.

For the case with purge flow, the bottom of the reduced cavity geometry is configured in AVBP as an inlet with an imposed mass flow rate equal to 0.9% of the average main passage mass flow at the inlet. The current implementation of this type of inlet in AVBP does not allow for turbulence injection, so the simulated purge flow is purely laminar at the inlet. To compute the mass flow target for this boundary condition, the average mass flow through the main passage was taken as $0.129 \text{ kg}\cdot\text{s}^{-1}$. With this, the cavity mass flow target is easily computed as $0.00116 \text{ kg}\cdot\text{s}^{-1}$. Dividing the cavity mass flow by the cavity inlet area gives the density times the velocity at the inlet as $1.6465 \text{ kg}\cdot\text{m}^{-2}\cdot\text{s}^{-1}$.

4.2.1 Meshes Used

The goal of the final mesh is to provide a wall resolved LES over portions of the domain with experimental data or relevant flow physics. As such, the hub wall after the tip and the blades up to about 60% of the span target a $y^+ \leq 2$, where y^+ is the wall-normal nondimensional coordinate relative to the wall of interest. With the strong acceleration seen over the suction side of the blades, however, the achieved is $y^+ \leq 5$. This most finely refined mesh will be referred to as Mesh P, for its use of prism layers at the wall. The prisms over the blade are generated with a first layer height of 0.0125 mm, and six total layers with a geometrical growth rate of 1.15. Prism layers with the same parameters are also used over the majority of the hub. Two precursor meshes to this exist, of increasing refinements with tetrahedral elements only. Mesh 1 was used to initialize the solution cheaply, and the solution was subsequently refined with mesh 2, and finally mesh P. This reduced simulation cost as the transient flows can be simulated much faster on coarse meshes.

Table 1 below lists the number of elements for each of these meshes for the geometries without the cavity (no cavity, NC) and with a shortened cavity (with cavity short, WCS). These meshes

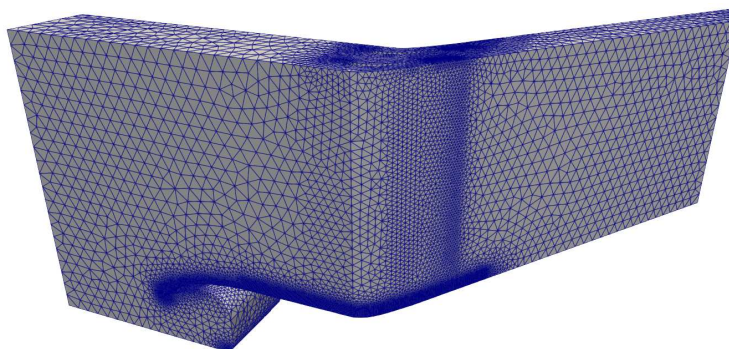
were produced using the CENTAUR grid generator². This software allowed for the easy import of test-specific geometries, region-specific mesh refinements, and the meshing process could also be submitted as a batch job to the CERFACS supercomputers (useful for the generation of extremely large meshes).

Table 1: Sizes of meshes used to converge results.

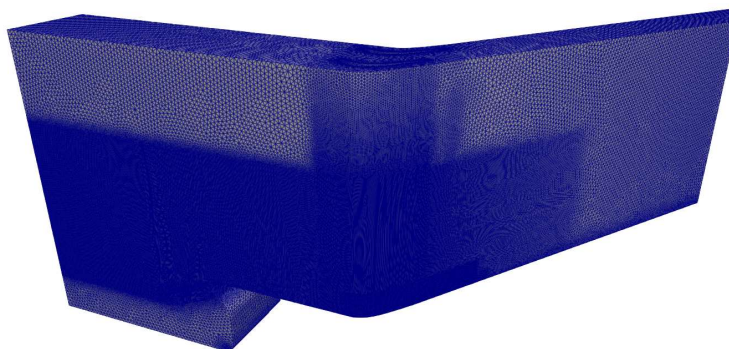
Mesh	Geometry	
	NC	WCS
1	8.74 M	12.23 M
2	180.10 M	181.82 M
P	172.68 M	176.64 M

In comparison with Mesh P, Mesh 2 targets a y^+ value of around 8 at the wall and has a greater cell count. This is because the shape of the prism cells allows for fewer cells over the surface with the same resolution in the wall normal direction, whereas the tetrahedral cells target a surface resolution on the same order as the resolution in the wall normal direction. No results will be presented on Mesh 2.

Figures 6a and 6b show Mesh 1 and Mesh P, respectively, for the no cavity case.



(a) Mesh 1, no cavity.



(b) Mesh P, no cavity.

Figure 6: Overall mesh comparison.

²<https://www.centaurosoft.com/>

Figure 6b shows the refinement region from the inlet to the blades up to 60% of the blade span, targeting the region where experimental data is available. This refinement region is key, as it drives the minimum sizes of turbulence that can be injected from the inlet; at the same time, it contains a huge number of cells and drives the cost of the simulation. For these simulations, the cell size is set to 0.5 mm in this region. Less obvious from this figure is the refinement in the endwall region (near the hub wall by the blades), where there is a cell size of 0.2 mm imposed to capture the vortex formation physics between the blades and the hub.

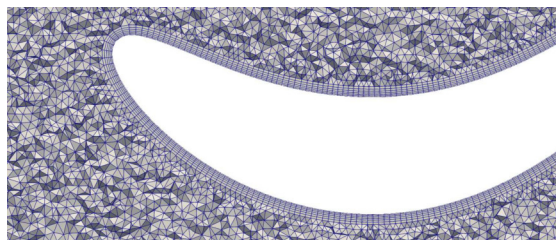


Figure 7: A crinkle-slice view of one of the blades at $z/H = 0.5$, Mesh P.

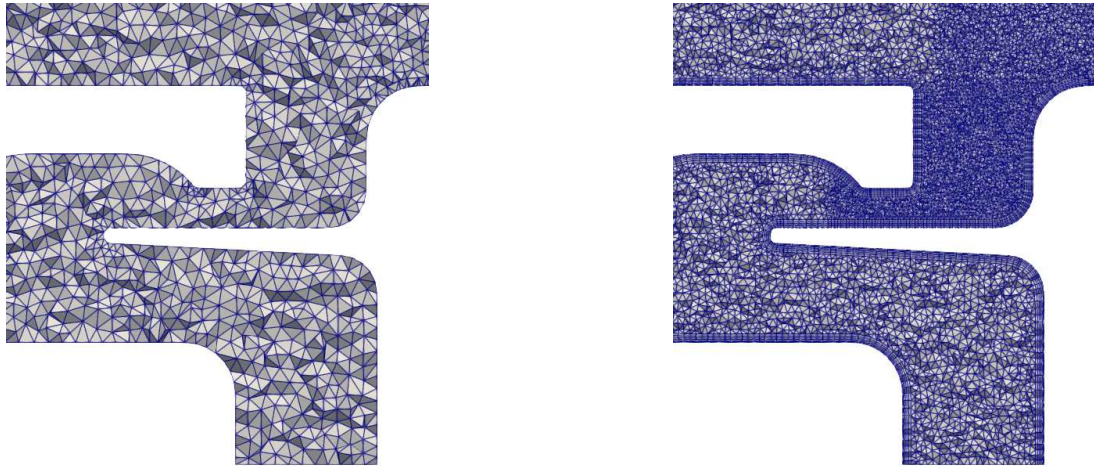
Figure 7 shows a closer look at the prism layers used on the leading edge of the blades. Prism layers are commonly used to accurately capture the boundary layer development and transition in LES, since they allow for refinement in the wall normal direction without a corresponding refinement in the wall tangent directions.



Figure 8: A crinkle-slice focused on one of the blades at $z/H = 0.5$, Mesh P, zoomed out.

Lastly, Figure 8 shows some regions of increased refinement, at the blade trailing edge and in the blade passage. The trailing edge refinement was selected a priori based on the experimental data and was chosen to try to better capture the dynamics of a potential trailing edge separation as well as unsteady wake phenomena.

The generation of the cavity mesh is done with the same refinement regions and parameters for all three meshes as in the no cavity case. The addition of the cavity is relatively straightforward. For the coarse case, the cavity is set such that it has the same resolution as the flow just outside the cavity, and all other parameters are the same as in Mesh 1 for the no cavity case (see Figure 9a). Mesh P also further refines the cavity exit, as there are expected to be recirculating flows, strong velocity gradients, and increased mixing in this region.



(a) Mesh 1, cavity zoom.

(b) Mesh P, cavity zoom.

Figure 9: Cavity mesh comparison.

Figure 9b above shows the refinement in the cavity. For the bottom of the cavity, the cell size is 0.5 mm, the same as in the main flow. Near the outlet, the cell size decreases to 0.2 mm to match the endwall refinement to capture the interaction of the cavity on this region. The cavity also includes the same six prism layers as on the hub to smooth these sections of the mesh.

4.2.2 Turbulence Injection

As mentioned previously, the SPLEEN LPT linear cascade has experimentally recovered turbulence statistics. Pastorino et al. [4] provide a method for calibrating hot-wire anemometry in the case of low-density transonic flows, where the wire’s sensitivity to density and velocity fluctuations make typical correlation methods invalid. At the reported standard operating conditions for the SPLEEN experimental set-up, the turbulence intensity at Plane 02 was determined to be 2.4% with an integral length of 12 mm. Typically, the integral length is not available from experimental data, and was determined via a zero-frequency extrapolation on the velocity spectra, after filtering. This extrapolated value was then used with a formula provided by Roach [8],

$$\Lambda = \left[\frac{E(f \rightarrow 0)|\bar{\mathbf{u}}|}{4|\overline{\mathbf{u}^2}|} \right] \quad (29)$$

to compute the integral length. Here, $E(f \rightarrow 0)$ is the power spectrum of the velocity extrapolated for zero frequency.

With an experimentally determined integral length, injecting relevant turbulence is fairly straightforward. In AVBP, there are a few methods to inject isotropic turbulence (such as that generated by a grid). The method selected for this project was Bailly’s method with a Passot-Pouquet spectrum [47], as described by P. Lepage [48] and implemented by A. Boudin in AVBP [49]. These methods have also been extended to allow for the injection of turbulence on a periodic domain, and for the injection of turbulence even when the primary flow direction is not perpendicular to the inlet (as in this report).

Bailly’s method is an extension of Kraichnan’s method [50]. Kraichnan’s method generates statistically stationary, homogeneous, isotropic turbulence using random Fourier harmonics se-

lected from a synthetic turbulent energy spectrum. This method is computationally inexpensive and produces a divergence-free turbulent field, which meets many of the typical ideal conditions for a turbulent LES inlet [51]. While this method is quite good, the fluctuating field does not generally satisfy the Navier-Stokes equations and so flows immediately after the inlet are non-physical. Bailly's method improves on Kraichnan's by using a uniform distribution of modes which can comply with any synthetic turbulent energy spectrum. A more detailed mathematical explanation on this method and Bailly's method are included in Appendix A. During the use of these injection methods in this internship, two bugs were discovered and corrected. These bugs are detailed in Appendix B.

In brief, the Passot-Pouquet spectrum in Bailly's method is constructed via:

$$E(k) = A \left(\frac{k}{k_e} \right)^4 \exp \left[-2 \left(\frac{k}{k_e} \right)^2 \right] \quad (30)$$

with A as the amplitude of the spectrum and k_e is the wave number associated to the most energetic length scale. Lepage [48] shows that by defining the turbulent kinetic energy as $TKE \equiv \frac{1}{2} u'_i u'_i = \frac{3}{2} U_p^2$ gives the constant A as:

$$A = \frac{16U_p^2}{k_e} \sqrt{\frac{2}{\pi}}. \quad (31)$$

The spectrum is defined for all wave numbers k with two factors, U_p and k_e . U_p controls the amplitude of the energy spectrum, and corresponds to the rms fluctuation of the velocity (assuming isotropic turbulence). This parameter is user-controlled to reach target turbulence intensity levels. k_e controls the position of the peak of the spectrum and its extent, and is related to the integral length scale, L_i , by:

$$L_i = \frac{\sqrt{2\pi}}{k_e}. \quad (32)$$

Within AVBP, the wave numbers, k , are generated based on the user input number of modes, N , as

$$k_j = \exp \left[\ln(k_{min}) + (\ln(k_c) - \ln(k_{min})) * \frac{j-1}{N-1} \right], \quad j = 1, \dots, N. \quad (33)$$

Here, k_{min} is determined based off the maximum turbulent length, L_{max} injected as

$$k_{min} = \frac{2\pi}{L_{max}}. \quad (34)$$

Likewise, the cutoff wave number, k_c , is determined based off the user input cutoff length as

$$k_c = \frac{2\pi}{L_c}. \quad (35)$$

Thus, with the user input parameters L_i, U_{rms}, N, L_{max} , and L_c , the injected turbulent spectrum is fully defined and is used to generate the N Fourier modes which become the input velocity perturbation. For this numerical study, these parameters are: $L_i = 12$ mm, $U_{rms} = 4.962$ m.s⁻¹, $N = 100$, $L_{max} = 65.29022$ mm, and $L_c = 1$ mm (twice the minimum grid resolution at the inlet).

4.2.3 Inlet Angle Determination

One critical factor in matching the experimental results is the incidence seen by the blades. Aside from the obvious effects that this has on the resulting velocity triangle of the turbine, it also has important implications for the flows seen around the airfoil. Anton and Wilberg [52] mention in their turbine rotor blade design thesis that the velocity distribution (and by extension, the isentropic Mach profile) will be greatly influenced by incidence, causing velocity peaks near the leading edge. Moreover, they mention that "usually negative incidence is less detrimental for the aerodynamic performance compared to positive incidence". This is corroborated by a previous numerical work by Zhang [53] which showed that the isentropic Mach profiles around the blade at the leading edge are more sensitive to positive off design angles of attack. The angle of attack also effects the separation of the the flow over the blade. For instance, if the angle of attack is too low on the blade, a pressure side separation is expected near the leading edge. Similarly, if the angle of attack is too high on the blade, a suction side separation is expected near the trailing edge.

For this numerical study, the experimental angle of attack is provided in the SPLEEN database. Initially, it seemed as though this angle could simply be imposed at the inlet of the computational domain. However, doing so revealed that the angle imposed at the inlet of the domain and that obtained at Plane 02 are quite different.

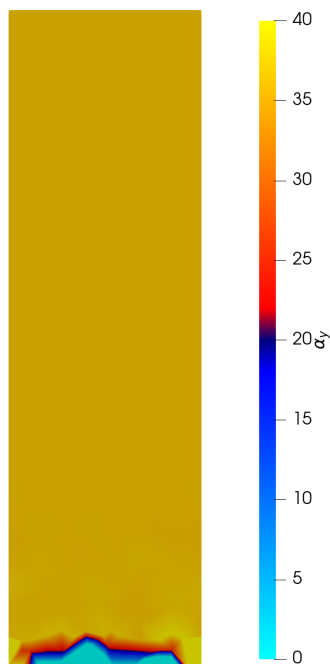


Figure 10: Instantaneous inlet angle distribution.

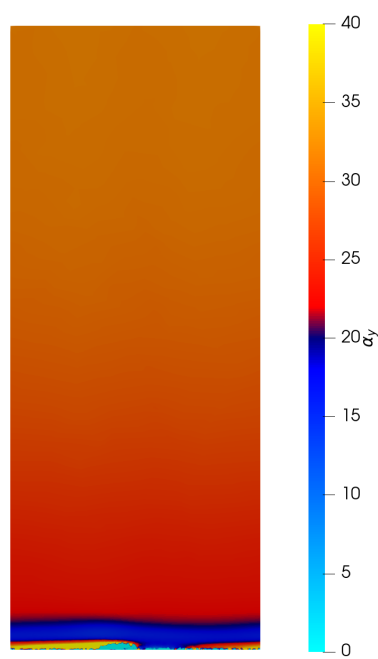


Figure 11: Instantaneous Plane 02 angle distribution using initial inlet angle.

Figures 10 and 11 are instantaneous results from the coarsest mesh, without turbulence injection. The angle is computed by taking the inverse tangent of the ratio of the w velocity and the u velocity. At the inlet, the flow angle 36.69° is prescribed uniformly (excluding the bottom at the no-slip wall), however the angle seen at Plane 02 is closer to 29° . Figure 11 also shows a strong decrease in the angle near the hub wall.

Considering again the computational domain, the reason for this becomes clear: there is an acceleration in the x direction due to the contraction of the domain in this direction. Figure 12 below from the same coarse simulation with the same initial angle emphasizes the magnitude of acceleration in the x direction, seen at a given instant.

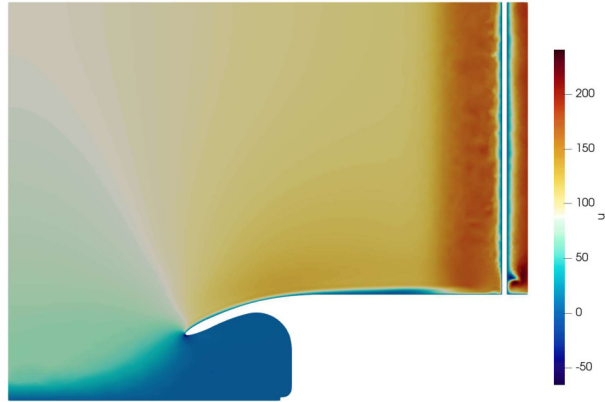


Figure 12: Instantaneous u velocity distribution in centerline of computational domain, y -plane view.

An unintended side effect may be linked to the effects of including the boundary layer trap in the domain. The included trap sees large circulating flows, which influences the development of the boundary layer over the hub, especially when the mesh is extremely refined. The trap also seems to induce a strong acceleration in the z direction (as seen in Figure 13) as the flow moves around the boundary layer trap and into the main passage. This induced acceleration may entrain additional flow nonuniformly throughout the main passage, leading to the angle distribution seen in Figure 13, where there is a significant reduction in the observed angle starting just after this velocity in the z direction.

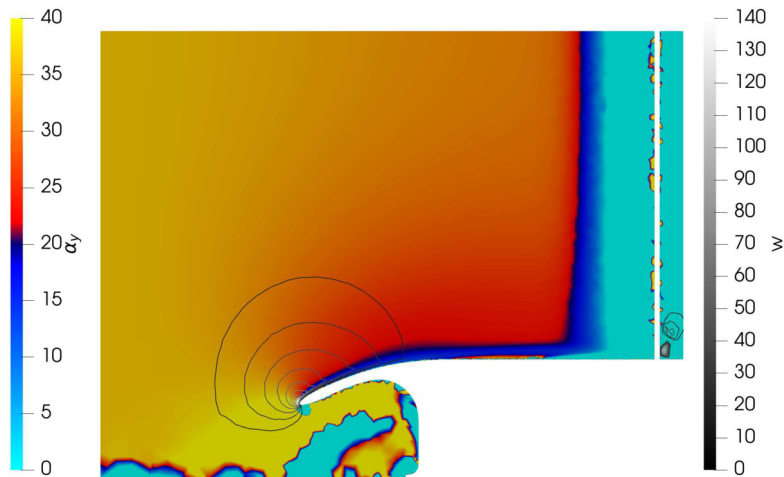


Figure 13: Instantaneous angle progression in xz midplane with contours of w velocity.

With the included boundary layer trap, prescribing an inlet angle to the computational domain is difficult as this angle is not recovered at Plane 02 where the experimental measurements are available. It is also possible that the inlet is too close to this geometrical feature and it is distorting the inlet. In the experiment, the acceleration due to the cavity is not a significant problem since the blades are adjustable and can be rotated as a group and aligned with the observed flow angle at Plane 02.

4.3 Results

In this section, the flows in each case are characterized and compared to each other and to experimental data when relevant. The flow in the region $z/H > 0.5$ will not be included in the analysis, as the experimental database does not include results here and the simulated domain is less refined in this region. First, the validation of the simulation against experimental data will be provided. Then, representative instantaneous results are shown, and are then time-averaged to show overall trends in the flow behavior. These time-averaged results are used to analyze the losses downstream of the blades. Lastly, a relatively novel method for visualizing turbulent structures and classifying their types is described and applied. All of the results presented here (unless otherwise mentioned) are time-averaged over at least 25 milliseconds, which is approximately seven flow through times. The flow through time, τ_f , is conservatively estimated by

$$\tau_f = \frac{L_x}{u_{x,2}}, \quad (36)$$

which is the length of the domain in the x direction, L_x divided by the velocity in the x direction at Plane 02, $u_{x,2}$. Here, $L_x \approx 0.475\text{m}$, and $u_{x,2} \approx 130 \text{ m.s}^{-1}$, averaged on the plane. These values give a flow through time of approximately 3.7 milliseconds.

For this analysis, the losses in the SPLEEN turbine cascade will be separated into two main groups: blade losses and endwall losses. In a real turbine, there are also losses incurred from tip leakage flows or other flows such as cooling flows. While the loss mechanisms for these different groups are not independent, separating them is useful to understand what parts of the flows are contributing to the reduction of the turbine's efficiency.

Blade losses, as the name suggests, comprises the losses due to the blades. One major contributor to the blade losses is the development of the boundary layer on the blade's surface. In a low-pressure high-speed turbine such as the SPLEEN linear cascade, it is expected that the incoming turbulence will trigger the turbulent transition of the boundary layer on the blades. In these simulations, however, this transition is not seen. Accurately predicting this transition is difficult and depends on the turbulent intensity as well as the scales in the incoming turbulence. Another major contribution to blade losses comes from the trailing edge of the blade, where the wake of the blade produces strong mixing effects downstream, which contribute to overall losses.

Endwall losses refer to the processes related to the boundary layer at the hub (and shroud) both before and after the blade passage. Within this, the hub/shroud boundary layer losses are the losses due to the friction processes generated from the boundary layers seen at the hub or shroud of the mainstream passage, both before and after the blades. These boundary layers are larger than those seen at the blades, due to the longer length over which they develop. However, Fiore [54] suggests that these boundary layer losses only account for about 2/3 of the observed endwall losses. These boundary layers also interact with the blades, producing secondary flow structures. These flow structures have been the focus of numerous studies, and a fairly recent review is available by Langston [55].

The first of these secondary flow structures to develop is the horseshoe vortex, which develops as the hub boundary layer is rolled up by the high pressure region of the leading edge of the blades. This horseshoe vortex travels down the blade passage, and the vortex generated on the pressure side is pulled by the pressure gradient towards the suction side of the nearby blade. The suction leg of the horseshoe vortex and the other shed pressure leg merge in the blade passage, forming the passage vortex. This strong passage vortex induces several other smaller vortices, notably the corner vortex (developed at the intersection of the blade and the hub) and the wall vortex (developed in the blade passage as the pressure side corner vortex is deflected to the suction side).

Figure 14 provides a schematic overview of these types of flow structures.

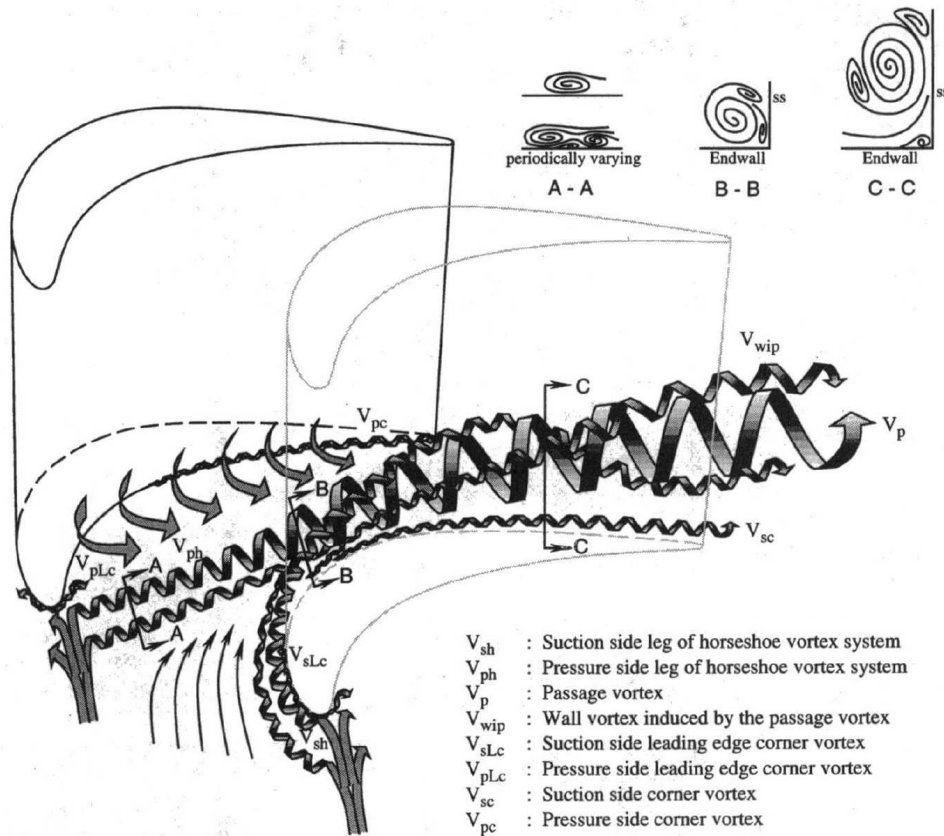


Fig. 8 Interpretation of the vortex flow pattern

Figure 14: Secondary flow identification in the blade to blade passage region [56].

While the development of these secondary flow structures does not inherently generate losses, the strong vortex cores are then accelerated through the blade passage, which induces a strong velocity gradient near the core, generating losses. Furthermore, these flow structures also contribute to increased mixing and to additional friction on nearby surfaces.

To visualize the flow in the turbine cascade, many of the following figures will show the isosurface of Q -criterion with $Q = 5E7 \text{ s}^{-2}$, taken from the averaged flow field solutions over

approximately seven flow through times (or 10ms). The time averaged flow field is used to generate the Q -criterion plots because the goal of the visualization is to isolate the large, time-independent vortical structures and filter out smaller vortical structures. On an instantaneous field, the turbulent flow has some vortical structures that would be identified by a given Q -criterion isosurface, but these are not of interest. Moreover, the large vortical structures do not vary too much in space, and so the time averaging procedure is effective for highlighting these coherent structures.

The Q -criterion is an invariant is defined as:

$$Q = \frac{1}{2} (\|\Omega\|_F^2 - \|S\|_F^2). \quad (37)$$

Here, the velocity gradient tensor, $\nabla U = S + \Omega$, is decomposed into its symmetric part, $S = \frac{1}{2} (\nabla U + (\nabla U)^T)$, the strain rate tensor, and its antisymmetric part, $\Omega = \frac{1}{2} (\nabla U - (\nabla U)^T)$, the vorticity tensor. While costly to compute over a large mesh, this tensor is useful as it identifies a vortex when $Q > 0$. Conceptually, this indicates that the square of the strain rate is greater than the square of the vorticity. The magnitude of Q indicates the strength of these vortical structures. Other methods for visualizing and identifying vortex structures are discussed by Jeong and Hussain [57].

4.3.1 Validation of LES Results

To match the experimental angle profile, the acceleration in the x direction can be reasonably predicted with the simple application of the conservation of mass in this direction. With this, the flow speed at Plane 02, u_{pl02} , can be estimated by

$$u_{pl02} = u_{in} \frac{A_{in}}{A_{pl02}}, \quad (38)$$

where A_{in} is the inlet area normal to the x direction, u_{in} is the velocity in the x direction at the inlet, and A_{pl02} is the area of Plane 02 normal to the x direction.

Knowing what the angle and Mach number should be at Plane 02, the isentropic relations can be used to estimate the u and v component at Plane 02 and then solve for the corresponding u_{in} , knowing that $v_{in} \approx v_{pl02}$. This provides a much more accurate starting point to which the angle can be fine tuned. Note also that here the angle is kept constant across the inlet plane, and a better agreement with the experimental data could be achieved with a variable angle.

Figures 15 and 16 below show the time averaged and plane averaged angle on Plane 02 as a function of blade span using the final selected angle, $\alpha_{in} = 46.5^\circ$ without the cavity, with turbulence injection. Here, this final value was fine tuned after using the equation provided above as an initial guess. This inlet angle was selected to produce results such that the angle of attack at $z/H = 0.3$ would match the experiment. The values shown in Figure 15 are averaged over approximately seven flow through times.

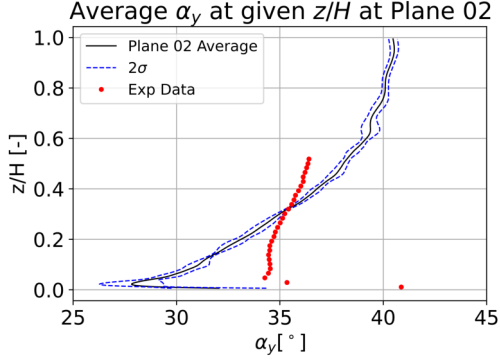


Figure 15: Plane 02 angle distribution, no cavity, LW.

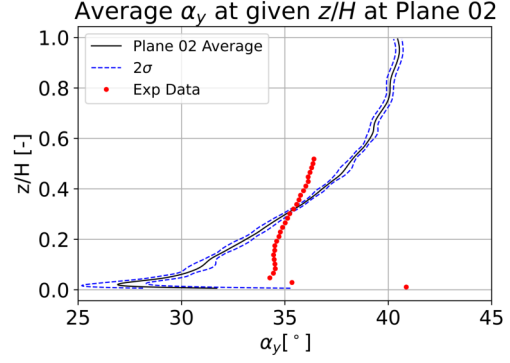


Figure 16: Plane 02 angle distribution, no cavity, TTGC.

At $z/H = 0.3$, the simulation produces an incidence very similar to that of the experiment's, indicating that the inlet angle imposed meets the goal of retrieving the correct angle of attack at this spanwise position. Below this height, however, the angle of attack observed in the simulation is much lower. This reduction in angle of attack is attributed to the effects of the boundary layer trap and the associated nonuniform acceleration. Given that the whole angle distribution is difficult to predict and is computationally expensive to determine, this angle was deemed to be sufficiently close to the experimental results. A key difference in these two results is that the angle of attack profile in the experiment is shown to vary much more gradually than in the simulation.

Another key parameter to match with the experimental data is the turbulence intensity (TI) and the associated turbulent integral length scales seen in the domain. To monitor the development of these parameters, two lines of probes are placed from the inlet to Plane 02 at $z/H = 0.25$ and 0.5 , centered on the inlet in the y direction. These probes are used to record the instantaneous velocity fields seen at these points during the simulation. With this data, the signal at each point is used to determine the local turbulence intensity by:

$$TI = \frac{\sqrt{\frac{1}{3} (u'_{x,rms}{}^2 + u'_{y,rms}{}^2 + u'_{z,rms}{}^2)}}{|\bar{\mathbf{u}}|}. \quad (39)$$

The root-mean-square (rms) components ($u'_{x,rms}$, $u'_{y,rms}$, $u'_{z,rms}$) are determined by

$$u'_{j,rms} = \sqrt{\frac{\sum_{i=1}^N (u_j^i - \bar{u}_j)^2}{N}}, \quad (40)$$

which is the same as square root of the variance over N measurements, where u_j^i is the i th measurement of a given velocity component, u_j . Then, the autocorrelation of the velocity vector is computed with these rms values in Python. Using the autocorrelation of the velocity, the first crossing of a set threshold value can be used to determine the turbulent time scale. Multiplying this turbulent time scale by the mean velocity gives the turbulent length scale [58].

For the simulated case with no cavity, the evolution of the turbulence intensity and the length scale are plotted below in Figures 17 and 18 as a function of distance from the inlet. The velocity signal used was gathered over approximately seven flow through times.

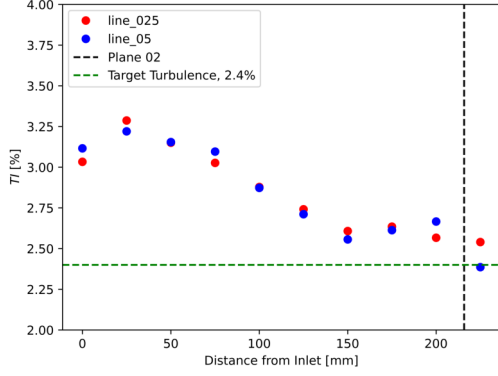


Figure 17: Turbulence intensity evolution, no cavity, LW.

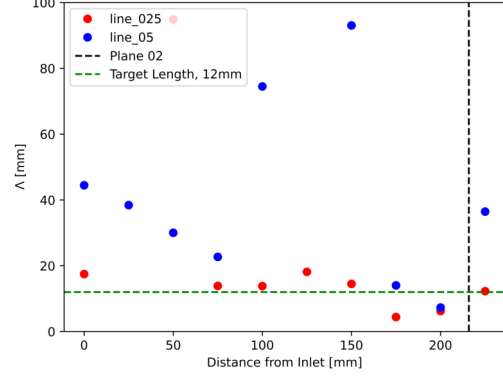


Figure 18: Turbulent integral length scale evolution, no cavity, LW.

As expected, viscous effects (both real and numerical) contribute to the overall decrease in turbulence intensity as the distance from the inlet increases. The evolution of the turbulent integral length scale is less well behaved, and some computed values are much greater than the expected values. This is due to the short signal that is being autocorrelated, and would improve with a longer signal. Overall, Figures 17 and 18 show turbulence intensities and turbulent length scales similar to those seen in the experiment, and indicates that the turbulence injection method is working as intended.

Another metric considered to match the simulation to the experiment is the isentropic Mach profile seen on the blades at a given height. This profile is important to match as it is related to the blade loading, the acceleration on the blade, and the angle of attack. The isentropic Mach number is computed via

$$M_{is} = \sqrt{\frac{2}{\gamma - 1} \left[\left(\frac{P_{01,fs}}{p} \right)^{\frac{\gamma-1}{\gamma}} - 1 \right]}, \quad (41)$$

where $\gamma = 1.4$ is the specific heat ratio, $P_{01,fs}$ is the freestream total pressure, and p is the local blade static pressure.

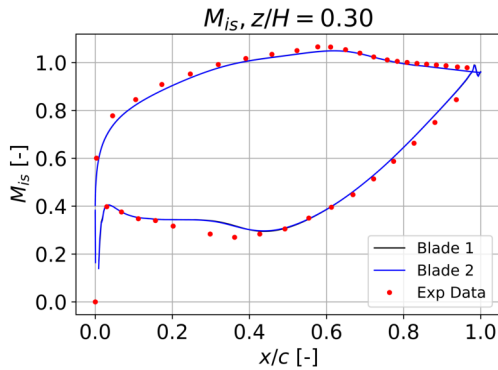


Figure 19: Isentropic Mach profile at $z/H = 0.3$, no cavity, LW.

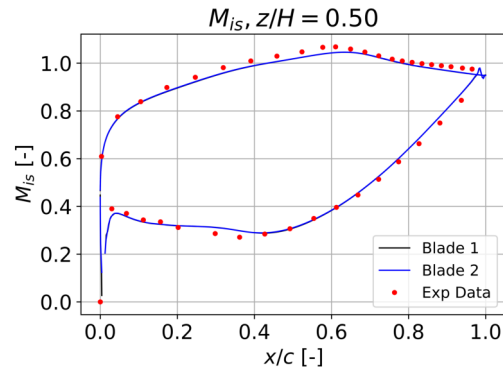


Figure 20: Isentropic Mach profile at $z/H = 0.5$, no cavity, LW.

Figures 19 and 20 show good agreement between the simulated blades and the experimental profile, and the two simulated blades produce almost the exact same curve, as expected for a well-converged simulation. A few differences are observed between these profiles, however. Firstly, the experimental profiles experience a greater acceleration over the suction side of the blade, reaching a greater maximum isentropic Mach number at a position slightly before the simulated ones. The numerical profiles also suggest a larger separated flow region on the pressure side of the blade than is seen in the experiment. Lastly, the numerical profiles show a strong acceleration at the trailing edge pressure side and a stronger deceleration on the trailing edge suction side than is seen in the experimental profile.

Very similar isentropic Mach profiles on the SPLEEN blades were obtained by Boudin [59], who also showed that LES overpredicted the pressure side separation region compared to the experimental data, even with a finer mesh than the one used in this project. His LES results also showed that the pressure side trailing side sees an isentropic Mach number slightly greater than observed in the experiment, as seen in Figure 19, and the suction side trailing edge sees a slightly reduced isentropic Mach number relative to the experimental data.

These same trends are also seen in Figures 21 and 22, which show the results of the same no cavity simulation using the higher order TTGC convection instead.

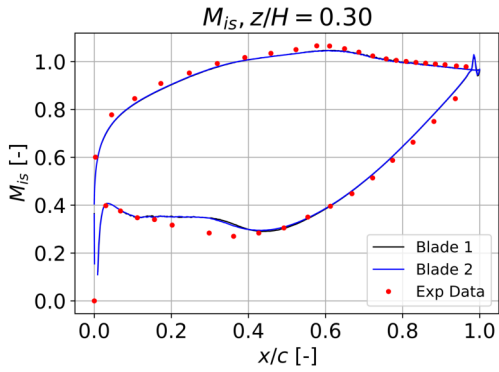


Figure 21: Isentropic Mach profile at $z/H = 0.3$, no cavity, TTGC.

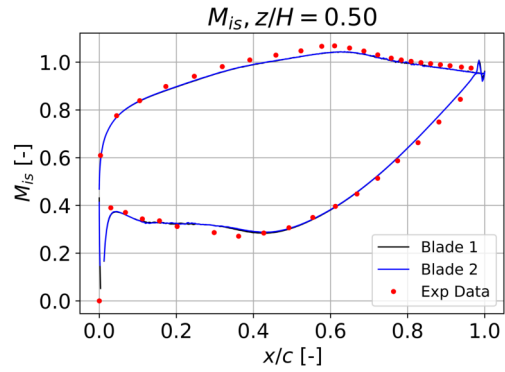


Figure 22: Isentropic Mach profile at $z/H = 0.5$, no cavity, TTGC.

Here, the TTGC scheme shows a slightly more pronounced separation on the pressure side of the blade, both for $z/H = 0.3$ and for $z/H = 0.5$. In either convection scheme, this too long separation on the pressure side of the blade for the $z/H = 0.3$ case is difficult to explain as the angle of attack at this blade span almost exactly matches the experimental results.

Overall, the angle profiles, the turbulence statistics, and the isentropic Mach profiles suggest that the simulation is operating at conditions reasonably close to the experiment, and so further analysis is representative of the actual flow topologies seen in the experiment. Since there are no notable differences between the LW and the TTGC convection scheme, the LW method will be used for the remainder of the report as it is less computationally expensive.

4.3.2 Investigation of Instantaneous Flow Fields

Here, the effects of turbulence modeling in the simulation are illustrated, and the effects of the inclusion of the boundary layer trap are discussed. To begin, Figure 23 below shows a sample instantaneous velocity magnitude field in the xz plane, where the plane is located at the midpoint of the inlet in the y direction.

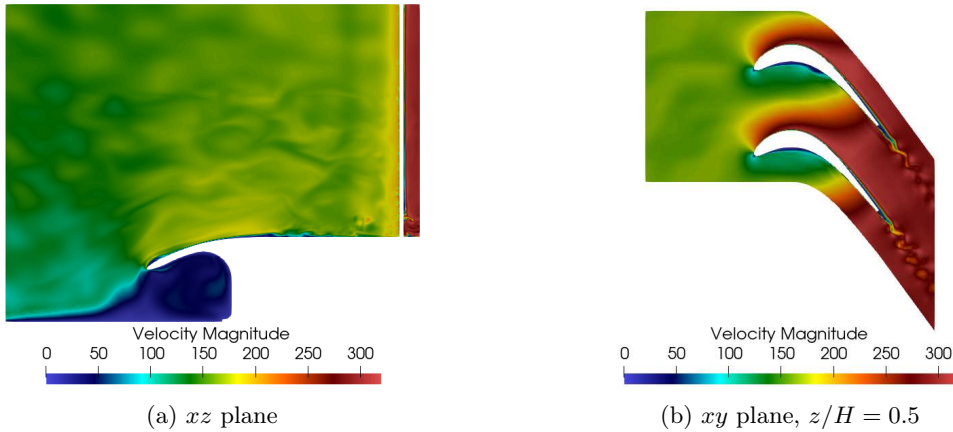


Figure 23: Instantaneous velocity magnitude field, no cavity.

Figure 23 highlights an important consequence of including the boundary layer trap. The inclusion of the boundary layer trap results in the formation of a recirculation region, which is important because it directly contributes to the stability and attachment of the boundary layer at the hub tip. This induces a slight "flapping", where the boundary layer oscillates up and down as the recirculation region occasionally leaks low velocity flow back into the main flow. These oscillations travel with the main flow along the boundary layer, and interact directly with the formation of the secondary vortices of interest. These oscillations are also seen for the cases with the cavity, as seen in Figures 24 and 25. Examining the case with purge flow, Figure 25 visually indicates that the purge flow is exiting the cavity and entering and interacting with the main flow, as expected. All of the instantaneous blade velocity fields in Figures 23b, 24b, and 25b show a large separation region on the pressure side of the blades. The flow over the blades also appears to be laminar, and a small separation region on the trailing edge of the suction side forms as well. The laminar flow over the blades leads to an unsteady, shedding wake.

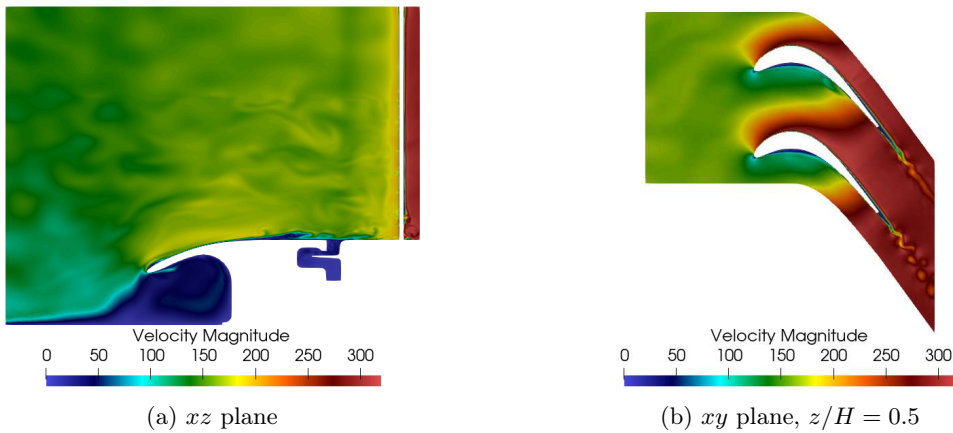


Figure 24: Instantaneous velocity magnitude field, cavity without purge flow.

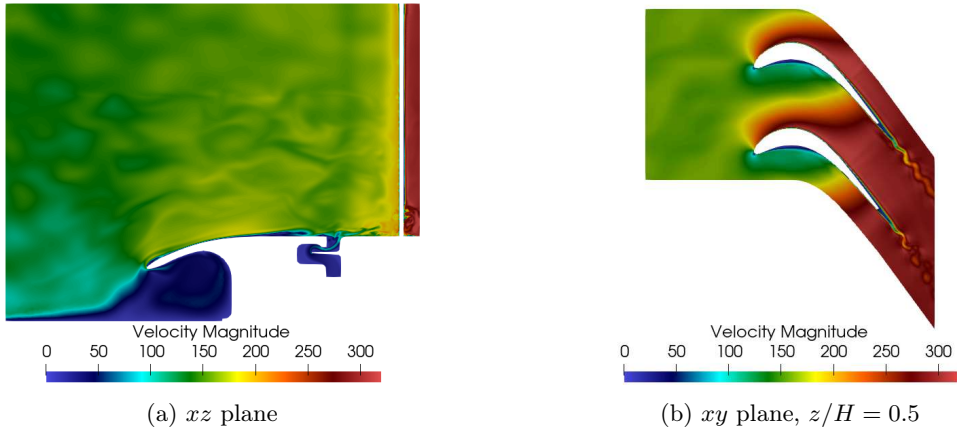


Figure 25: Instantaneous velocity magnitude field, cavity with purge flow.

4.3.3 Characterization of Time-Averaged Flow Fields

To characterize the development of vortices seen in the cases, the following figures show the isosurface of Q -criterion at $Q = 5E7 \text{ s}^{-2}$, colored by vorticity in the x direction to indicate the rotational direction of the vortical structure. These results (and subsequent figures) are produced from time averaged flow fields over approximately seven flow through times.

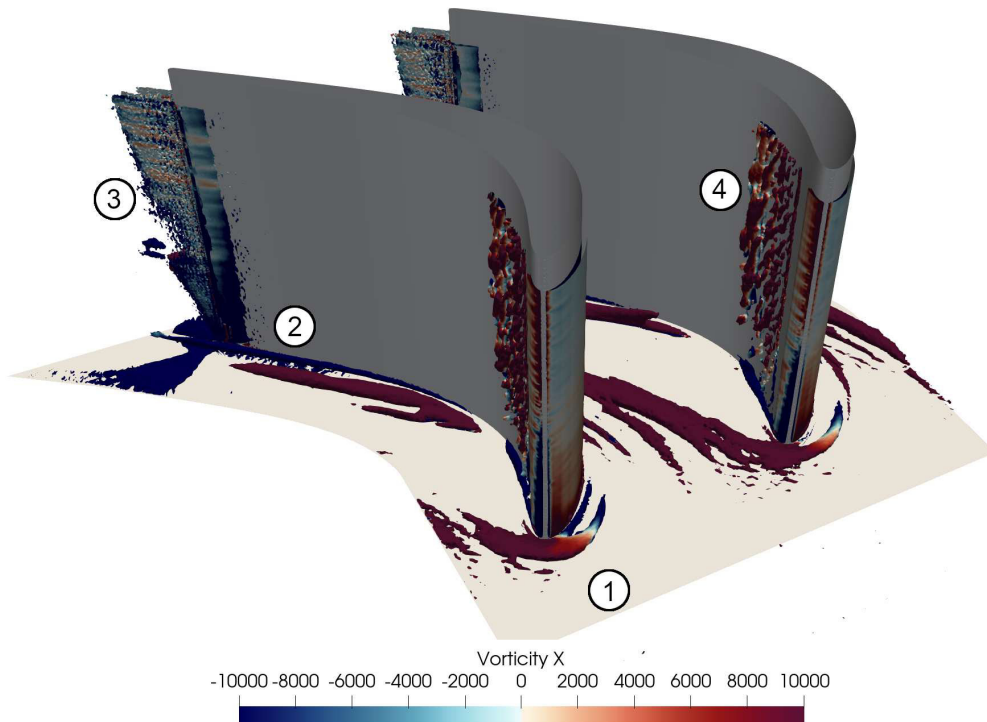


Figure 26: Q -criterion isosurface, $Q = 5E7 \text{ s}^{-2}$, no cavity.

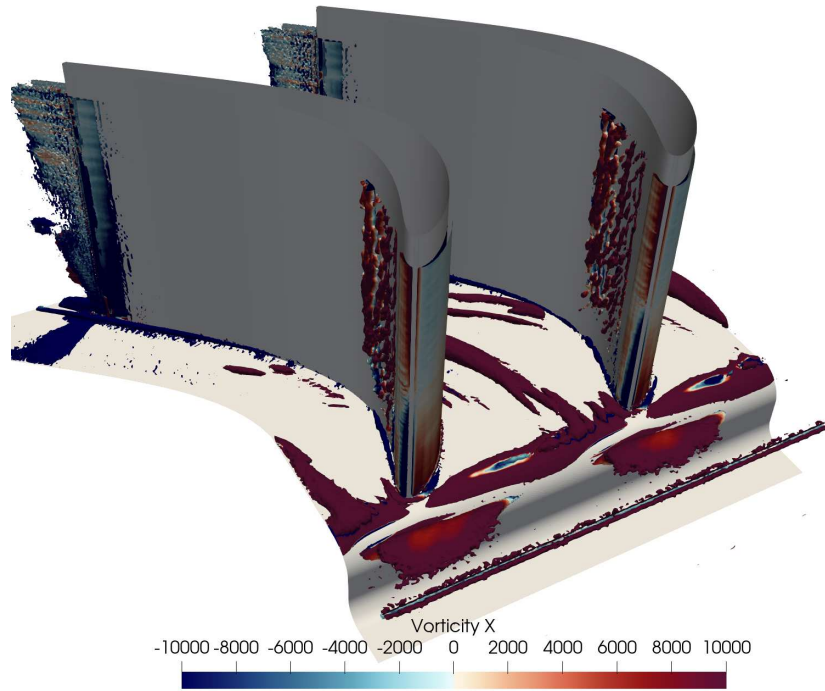


Figure 27: Q -criterion isosurface, $Q = 5E7 \text{ s}^{-2}$, cavity no purge flow.

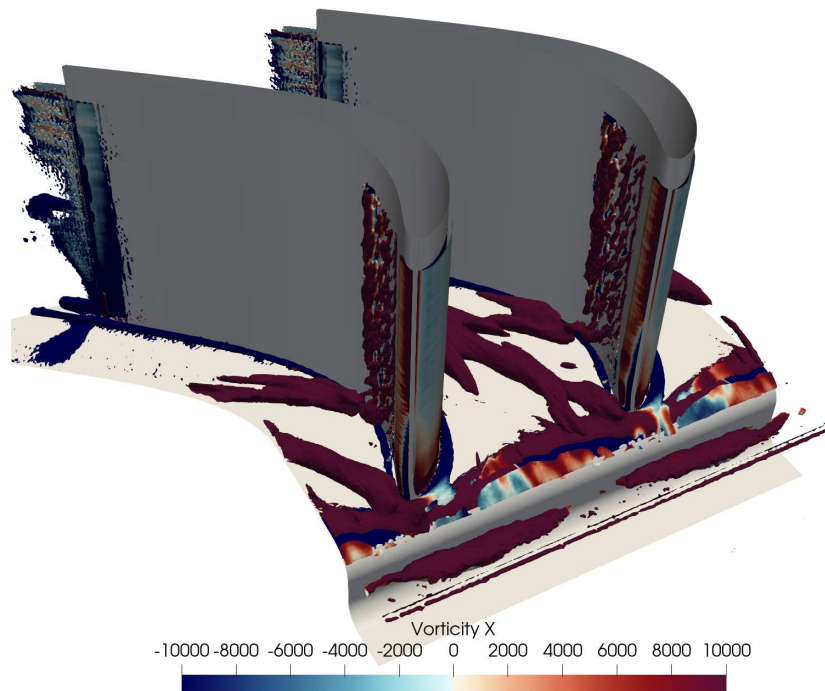


Figure 28: Q -criterion isosurface, $Q = 5E7 \text{ s}^{-2}$, cavity with purge flow.

Qualitatively, the flow in the simulated turbine cascade reproduces the same secondary flows of interest, including the horseshoe vortices (label 1), the corner vortex (label 2), and the trailing shed vortices (label 3), with the numbers indicating the structures as seen in Figure 26. The expected behaviors are observed, such as the movement of the pressure side horseshoe vortex into the suction side of the adjacent blade. Figures 26, 27, and 28 all suggest a separation region on the pressure side of the blade near the leading edge (label 4).

In general, the introduction of the cavity geometry has a strong impact on the flow patterns in the hub region observed in the simulation. Secondary flow structures begin to develop at the end of the cavity and are already larger than in the case without the cavity. Comparing Figure 27 with Figure 26, most of the patterns on the blades or the blade wakes are not strongly affected by the inclusion of the cavity. Instead, the main changes are those closely related to the endwall. Notably, there is no clear "rollup" of vortex structures at the leading edge of the blade at this Q -criterion isosurface, and instead it seems as though the passage vortex begins forming at the side of the cavity closest to the blades.

The cavity itself allows for some slight vortex structure formation inside the cavity as it exits as well as for some other vortex structures centered around the blade leading edges slightly deeper in the cavity. This is attributed to the potential effect of the blades. The potential effects leads to the distortion of the vortical structures forming over the top of the cavity as different portions of the cavity see flow into or out of the cavity.

Adding the purge flow has a noticeable effect on the topology of the flow in the blade passage, as seen in Figure 28, as the same Q -criterion isosurface is larger. This isosurface is also less organized as more smaller vortices escape from the cavity to join the passage vortex. These additional vortices disrupt the formation of the horseshoe vortex on the pressure side, strengthening it and inducing movement towards the other blade's suction side earlier in the blade passage. Examining the corner vortex formed in Figure 28, this structure develops almost immediately after the leading edge, and is more pronounced on the pressure side relative to the no cavity case and the cavity case without purge flow. This figure also suggests a link between the vortex structures in the separation region with the development of additional vortical structures that leave the blade to join the passage vortex.

Downstream of the blades, nearly all of the canonical secondary flow structures can be clearly seen. Figure 29 highlights how these structures have fully developed as they exit the blade passage in the case without the cavity.

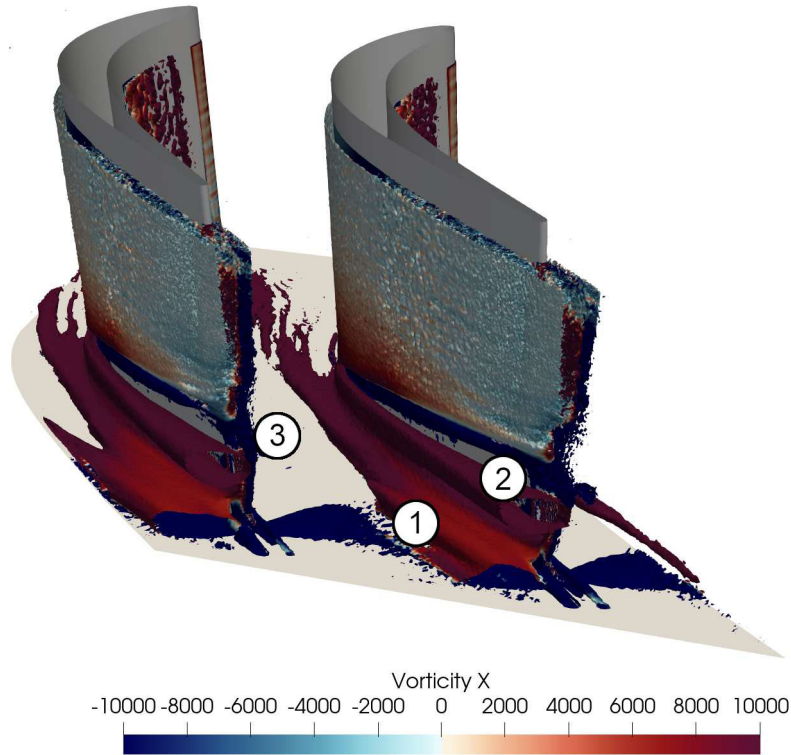
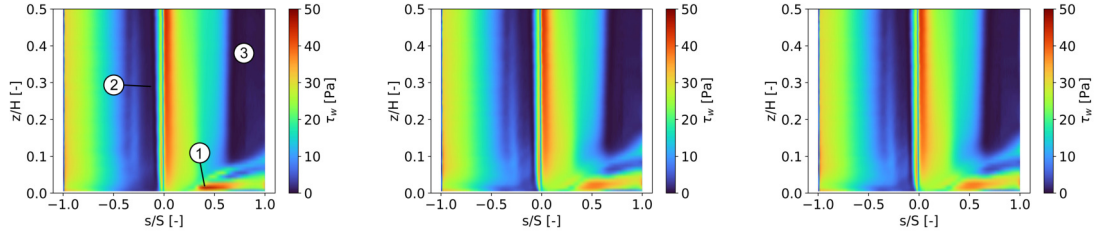


Figure 29: Q -criterion isosurface, $Q = 5E7 \text{ s}^{-2}$, colored by vorticity, view upstream, no cavity.

The hub passage vortex can be identified in Figure 29 (label 1) by its large size and its migration towards the blade suction side. The wall-induced vortex can also be seen (label 2) as it generates next to the strong passage vortex. Near the blade trailing edge, many of the secondary flows combine and the structures lose their otherwise clear forms. Here, the trailing edge wake vortices (label 3) can also be clearly seen in the form of large structures in the blade spanwise direction. The interaction of these spanwise structures with the flow-oriented structures leads to complex, three-dimensional vortical shapes indicative of increased mixing.

Secondary flow features can also be inferred from the skin friction plot on one of the unwrapped blades (Figure 30), as the strong passage vortex induces flow detachment/attachment on the surface of the blade. Examining spots of high magnitude wall shear stress indicates regions with high velocity gradients near the wall. This is characteristic of secondary flow features. For instance, in Figure 30a, the spot on the suction side near approximately $s/S = 0.4$ (label 1) corresponds to the merging of the pressure side horseshoe vortex with the suction side horseshoe vortex, which generates an increase in friction. Furthermore, the pattern seen for $s/S > 0.5$ and $z/H < 0.15$ is indicative of the development of an induced wall vortex and corner vortex, where the shear stress reduces above and below the main passage vortex. Note that the small disturbances in the skin friction coefficient over the leading edge ($x/C = 0$) in these figures are due to the algorithm for the blade unwrapping procedure; the skin friction varies continuously and smoothly in the simulation. These skin friction plots are also useful to highlight regions where the flow is detached. For instance, in Figure 30a, on the suction side for $-0.2 < s/S < -0.05$ (label 2), there is a reduction in the wall shear stress due to the separation of the flow on this



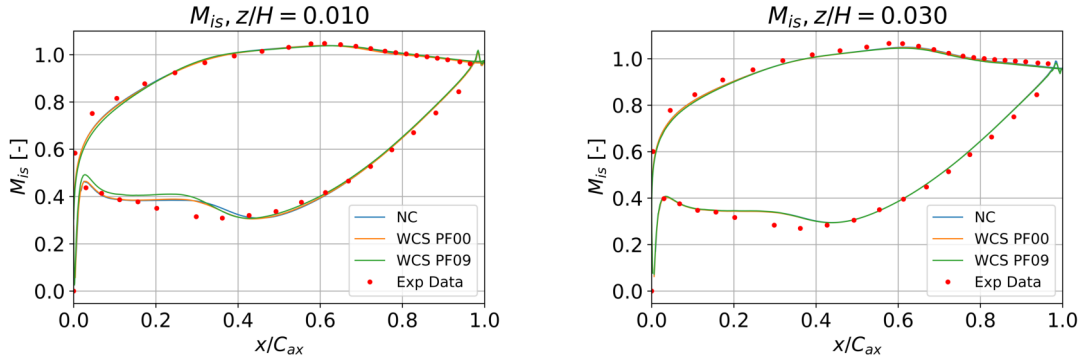
(a) Unwrapped blade skin friction, no cavity. (b) Unwrapped blade skin friction, cavity without purge flow. (c) Unwrapped blade skin friction, cavity with purge flow.

Figure 30: Blade skin friction comparison, negative x/S is the pressure side.

surface. Likewise, for $0.6 < s/S < 1.0$ at $z/H > 0.1$, there is a separation on the suction side of the blades (label 3).

In general, all three figures show a similar starting position for the pressure side separation and for the suction side separation region. The dark band seen on the pressure side separation in Figure 30a does appear to become lighter as the cavity is added, and lightens further as the purge flow is added, showing the flow is reattaching sooner for $z/H < 0.2$ with the cavity. Figure 30b also shows a reduced wall shear stress in comparison with Figure 30a, which could be because the altered starting position for the pressure side horseshoe vortex for the case with the cavity reduces the friction generated when the two horseshoe vortices merge on the suction side. With the addition of the purge flow in Figure 30c, the two bands (3) on the suction side for z/H move noticeably upwards and spread out. Additionally, the purge flow affects the shear stress pattern on the pressure side right from the leading edge, strongly reducing the separation effects seen in the other figures.

Of course, the different secondary flows also have some influence on the isentropic Mach number profiles seen on the blades. Figure 31 below shows the isentropic Mach number profiles at heights $z/H = 0.1, 0.3$. Above $z/H = 0.3$ these plots are virtually indistinguishable.



(a) Isentropic Mach number profiles, $z/H = 0.1$. (b) Isentropic Mach number profiles, $z/H = 0.3$.

Figure 31: Comparison of isentropic Mach number profiles.

Figure 31a shows how the purge flow affects the isentropic Mach number distribution; with this the isentropic Mach number on the pressure side of the blade increases noticeably, and the separation zone on this same side also reduces. Another interesting feature from this low blade

span height is that although the flow acceleration at the beginning of the suction side of the blade does not match well with the experimental results, the trailing edge side of the suction side accurately predicts the isentropic Mach number. Figure 31b shows effectively no difference between the cases, further emphasizing that the cavity effects are confined to the very near wall region.

4.3.4 Cavity Effects on Time-Averaged Flow

In order to study how the flow is perturbed by the cavity on average, Figures 32 and 33 showcase how the average streaklines generated just before the cavity at a height of 0.5 mm are affected by the introduction of the cavity and the activation of the purge flow. Left to right in both of these figures shows the no cavity case, the cavity case without purge flow, and the cavity case with 0.9% purge mass flow. These streaklines are colored by the magnitude of the velocity at the given position.

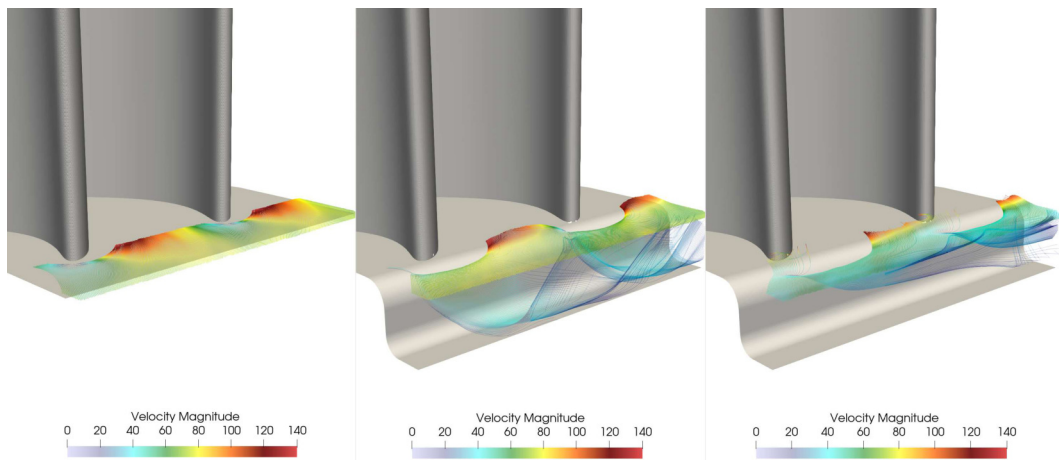


Figure 32: Cavity streakline perturbation.

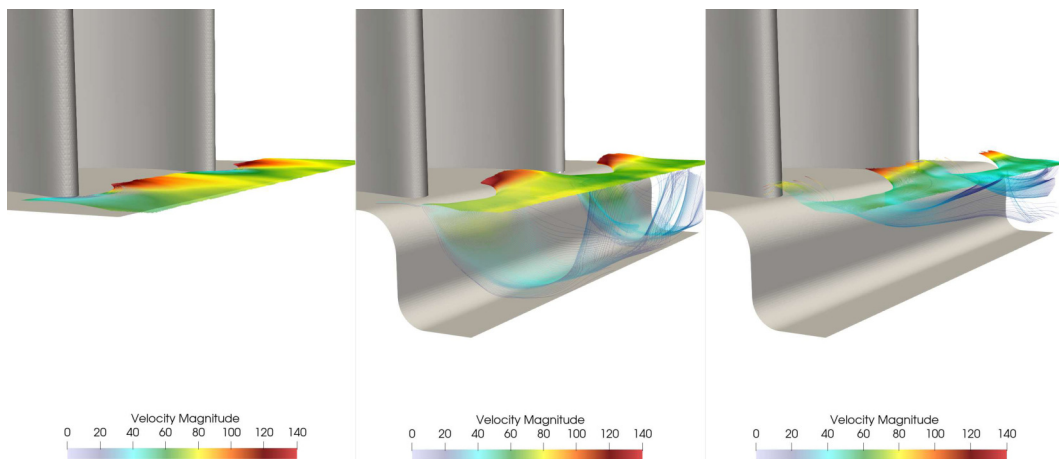


Figure 33: Cavity streakline perturbation, view down cavity.

Compared to the no cavity case, the velocity magnitude seen in the same region for the cavity case without purge flow is not strongly affected, as seen in Figure 32. The boundary layer sees a strong potential effect from the leading edge of the blades, which directs some of the boundary layer flow into the cavity for the case with 0% purge mass flow. This redirected flow generates the cavity flow recirculation as seen in the center of Figure 33. With 0.9% purge mass flow, however, the velocity seen in flow over the cavity is reduced, which suggests that the purge mass flow is pushing the incoming flow up above this position. Additionally, the shape of the recirculation region in the cavity is modified with the purge mass flow. While the same potential effect directs some of the flow into the cavity, the purge mass flow overcomes this effect. Correspondingly, the circulation region seen in the cavity is confined to the top to allow for the purge mass flow to escape from the cavity. The right of Figure 33 clearly shows how purge flow prevents the ingestion of the main flow into the cavity, as intended.

This boundary layer flow has a strong affect on the development of the horseshoe vortex formation, as seen in Figure 34 which shows the difference in Q -criterion structures with an isosurface at $Q = 5E7 \text{ s}^{-2}$. Left to right: no cavity, cavity 0% purge flow, cavity 0.9% purge mass flow.

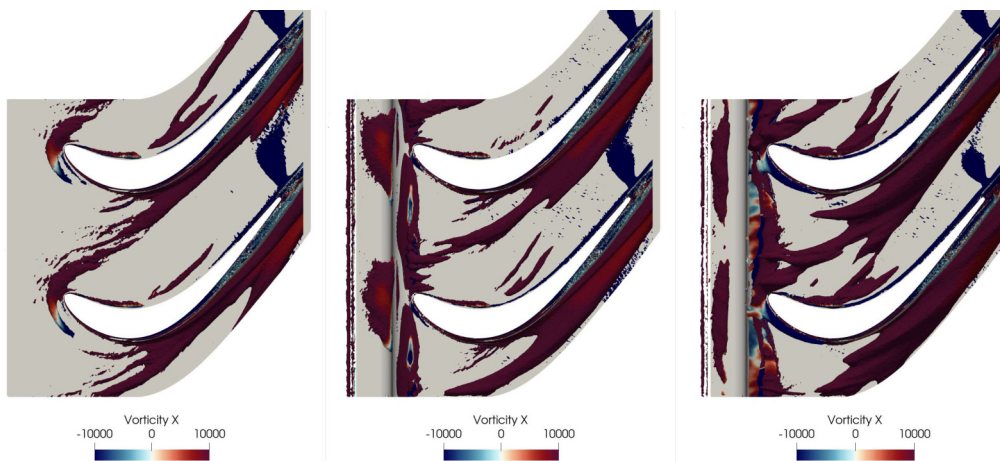


Figure 34: Vortical structures comparison, Q -criterion isosurface at $Q = 5E7$, colored by vorticity in x direction.

Figure 34 shows the obvious effect of the cavity on the development of the horseshoe vortex. The cavity's position is close enough to the leading edge of the blades such that this vortex shape is almost detached from the leading edge of the blades. This detachment of the suction side horseshoe vortex leads to a larger passage vortex, as seen in the center and right of Figure 34. Additionally, this figure emphasizes how the purge mass flow of 0.9% strongly influences the formation of vortical structures in the blade passage, as many more vortices at the same Q -criterion isosurface are identified in the right of Figure 34.

This figure also shows how the structure of the flow within the cavity changes as suggested by Figure 33, where adding purge mass flow constrains the circulation in the cavity to the region nearest to the incoming flow, allowing the purge flow to escape. Note also that each set of two blades in Figure 34 see the same general flow topology, which further indicates that the simulations are well converged and behaving as expected. Moreover, as the domain is periodic, this suggests that a full cascade would see these turbulent structures developing at each blade.

Lastly, Figure 35 shows the overall development of turbulent kinetic energy, TKE, looking

down the blade passage. Each of the images, from left to right are the no cavity case, the cavity case without purge flow, and the cavity case with 0.9% purge mass flow.

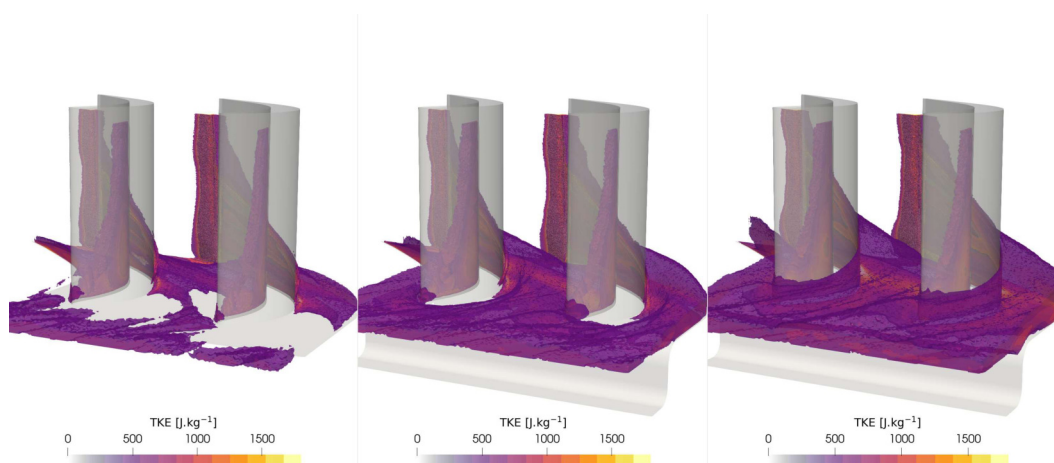


Figure 35: TKE development in blade passage.

Figure 35 shows a threshold for cells with TKE greater than 500 J.kg^{-1} in the domain. Doing so shows the intuitive effect of adding the cavity: there is increased turbulent kinetic energy in the blade passage, as expected. This increased TKE indicates greater mixing in the flow as the value increases. Moving from the center of Figure 35 to the right of the figure highlights how the addition of purge flow generates a strong increase in TKE overall. Here, not only does the affected region of the blade passage increase, but the peaks in TKE also increase. Recalling the shapes of the passage vortex, it can be seen that the passage vortex in each case is contributing to the a region of increased TKE. This is intuitive: the mixing and bursting effects of the large passage vortex generate turbulent energy.

4.3.5 Comparison of Plane 06 Downstream of Blades

With the overall flow features described in the cases, the next step is to characterize how these features affect the losses downstream of the blades at Plane 06, located $0.5C_{ax}$ downstream of the trailing edge. One metric for determining how these secondary structures have affected the losses is the energy loss coefficient. The energy loss coefficient, ξ , is defined [38] at this plane as:

$$\xi = 1 - \frac{1 - \left(\frac{P_6}{P_{06}}\right)^{\frac{\gamma-1}{\gamma}}}{1 - \left(\frac{P_6}{P_{01,fs}}\right)^{\frac{\gamma-1}{\gamma}}}. \quad (42)$$

Here, P_6 is the static pressure at Plane 06, and P_{06} is the total pressure at Plane 06. $P_{01,fs}$ is the freestream total pressure at Plane 01, here taken to be the imposed total pressure at the inlet, 9000 Pa. γ is the ratio of specific heats for air, taken as $\gamma = 1.4$. This coefficient is useful as it contextualizes the losses, which manifest as a decrease in total pressure at Plane 06.

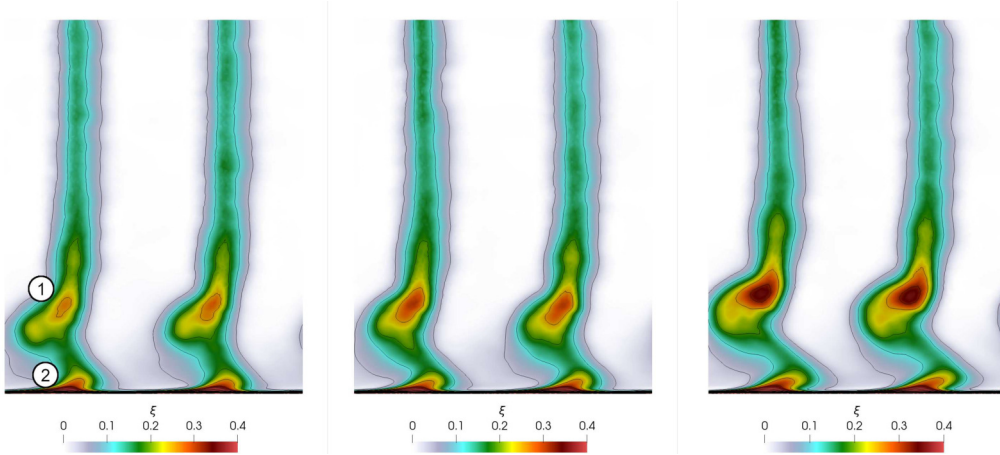


Figure 36: Plane 06 pressure loss coefficient plots.

Figure 36 shows the contours of the pressure loss coefficient at Plane 06 without the cavity, with the cavity, and with the cavity and purge flow, from left to right. This figure also allows for the clear identification of two main loss regions, one between interaction of the passage vortex and the wall induced vortex (label 1), and the other near the corner vortex (label 2). As expected, ξ increases as the cavity is included, and further increases as the purge flow is added. It is also observed that the regions of high ξ move upwards as the cavity effects are included. Considering the right of Figure 36, the upwards movement of the loss region associated with the passage vortex can be explained by the fact that the cavity flow introduces some momentum to the starting horseshoe vortex in the $+z$ direction.

Another useful quantity is the secondary velocity, which is the velocity in the plane of interest that is not aligned with the ideal flow direction. Here, if the turbomachine was perfect, the flow at Plane 06 would be uniformly and completely turned at the metal outlet angle, $\beta_{m,out}$. In reality, the velocity vector at Plane 06 can be projected onto this ideal velocity direction ($\hat{\mathbf{u}}$), and the secondary velocity vector can be determined.

$$\hat{u} = \cos(\beta_{m,out}), \hat{v} = 0, \hat{w} = -\sin(\beta_{m,out}) \quad (43)$$

$$u_{sec} = 0, v_{sec} = v, w_{sec} = u\hat{w} + w\hat{u} \quad (44)$$

The secondary velocity vector allows for the nonidealized flow velocities to be characterized on a given plane. A plot of these vector directions scaled by their magnitude overlaid on the energy loss coefficient for each case is presented in Figure 37.

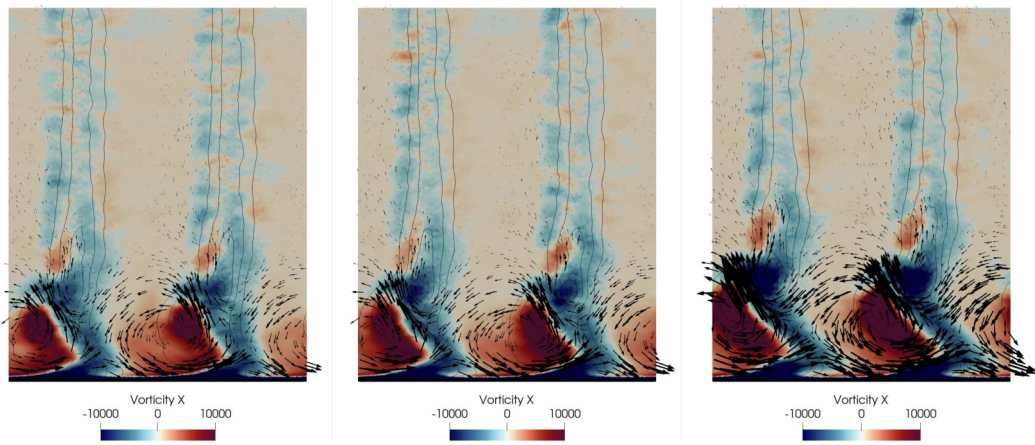


Figure 37: Plane 06 vorticity with secondary velocity directions.

Figure 37 shows the previous loss contours overlaid with black vectors in the secondary velocity directions, and the vorticity in the x direction (plane normal). This highlights how the intensity of the vortex cores increases with the introduction of the cavity and the purge flow, and also identifies how the high loss coefficient regions are directly related to regions where strong vortices of opposite signs are interacting. Additionally, the shapes of these vortex regions deform from the no cavity case. In the no cavity case, the positive vorticity region in the center (the passage vortex) is very circular without defects. As the cavity is included, this shape begins to deform slightly, bending inwards as the induced blade vortex gains strength. When the purge flow is activated, the central passage vortex is highly deformed, and both the corner vortex and the blade vortex are pushing against it.

Lastly, Figure 38 shows how the previous loss contours are related to regions of TKE.

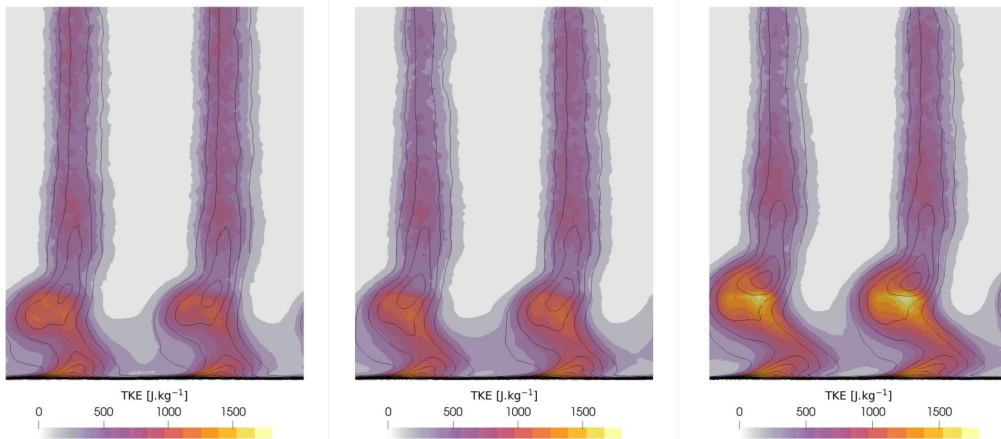


Figure 38: Plane 06 TKE with ξ contours.

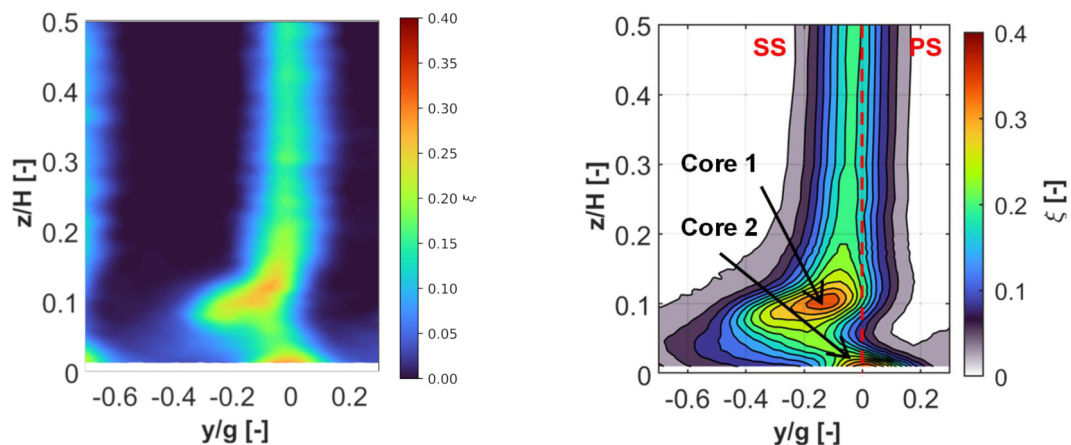
Here, it should be noted that the regions with highest ξ are not directly superimposed with the regions of highest TKE, though they are spatially related. Instead, these peaks in TKE coincide with regions where there is a strong gradient of the vorticity in the x direction from

Figure 37. In this way, Figure 38 highlights the blade passage vortex and the corner vortex as regions of high turbulent activity.

4.3.6 Comparison to Experimental Data

As mentioned previously, the experimental data available for comparison is only the no cavity case, as there were not any experiments performed with the cavity or with purge flow and without the wake generating rotating bars. The experimental data presented here is time-averaged over 3 seconds, considerably longer than those from the simulation.

Firstly, the no cavity loss contours at Plane 06 are compared with the experimental results in Figure 39.



(a) Energy loss coefficient, ξ , at Plane 06, no cavity.

(b) Energy loss coefficient, ξ , at Plane 06, experimental [45].

Figure 39: Plane 06 energy loss coefficient comparison to experimental results.

Figure 39a was created by manually scaling Plane 06 results such that it shared the same axes lengths with Figure 39b; as such, only the relative distances and shapes should be compared. With this in mind, the two are in good agreement with the overall shape of the loss curves. Both figures identify two loss cores, and show relatively the same positions between them, and appear to have comparable magnitudes of loss coefficient.

An important characterization of the flow at the outlet of the blades is the actual turning angle, β . This angle is computed as

$$\beta = \arctan\left(\frac{v}{u}\right), \quad (45)$$

and the deviation from the ideal turning angle, $\Delta\beta$ is calculated as the difference $\beta - \beta_{m,out}$. Figures 40 and 41 are pitch averaged over Plane 06 and show the overall effects of these secondary structures from the different cases relative to experimental data obtained without the cavity at Plane 06. Here, the labels "NC" are for the no cavity case, "WCS PF00" for the cavity case with no purge flow, and "WCS PF09" for the cavity case with 0.9% purge mass flow.

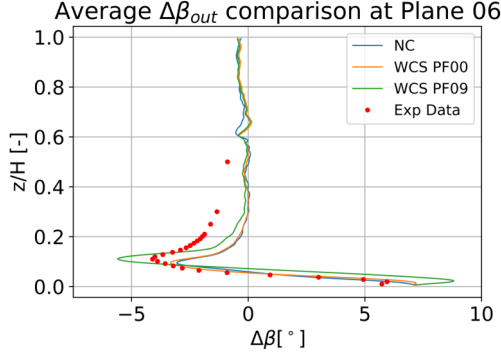


Figure 40: Plane 06 pitchwise averaged deviation from ideal turning angle.

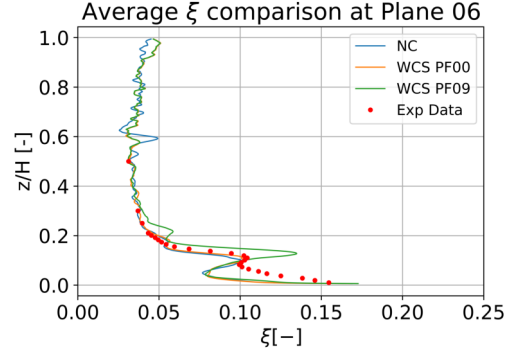


Figure 41: Plane 06 pitchwise averaged ξ .

Figure 40 shows fairly good agreement of $\Delta\beta$ between the simulated no cavity case and the experiment, which was not initially expected since the inlet angle distribution varies by more than 5° at points. Notably, the region below $z/H = 0.1$ is in very good agreement, and the z/H position of maximum absolute deviation is well predicted around 0.1, although the magnitude of this deviation is off by about 1.5° .

Figure 40 also shows that the turning angle at the outlet of the experimental data far from the endwall appears to differ significantly from the metal angle, while the simulated results all agree that the outlet angle at Plane 06 far from the endwall should be almost exactly the metal angle. Comparing the cases, the previous trends are further supported by Figure 40. As the cavity effects are included, the turning angle at the outlet decreases slightly but is overall not strongly perturbed, and when the purge flow is activated the turning angle is strongly affected, both increasing overturning and underturning seen by the flow close to the hub.

The outlet turning angle deviation is well complemented by Figure 41, which shows that the losses predicted for $z/H \geq 0.1$ are extremely accurate for the no cavity case. Whereas Figure 40 shows good agreement between the simulation and the experiment for $\Delta\beta$ below $z/h \leq 0.1$, Figure 41 shows that all of the sims underpredict the losses in this region.

Both Figure 40 and Figure 41 show a perturbation in the plots at $z/H = 0.6$, which is expected since the mesh quality changes fairly quickly at this point.

4.3.7 Categorization of Turbulent Structures

Since LES can capture the turbulence anisotropy in the spatial domain, analysis on this anisotropy can provide additional information as to the types of turbulent structures seen that would otherwise be unavailable for a RANS simulation. As suggested by Emory [60], predicting the amount and type of anisotropy is critical for accurate numerical simulation of complex flows. Emory defines the anisotropy from the Reynolds stress anisotropy tensor,

$$a_{ij} = \frac{\overline{u'_i u'_j}}{2TKE} - \frac{\delta_{ij}}{3}, \quad (46)$$

where $TKE = \frac{1}{2} \sum_{n=1}^3 \overline{u'_n u'_n}$. The Reynolds stress anisotropy tensor, a_{ij} , can be diagonalized to extract three eigenvalues and three eigenvalues of turbulence anisotropy. Extracting these invariants was originally introduced by Lumley in 1977 [61] in order to study the return to isotropy of homogeneous turbulence. These three eigenvalues, λ_1 , λ_2 , and λ_3 are generated at each point and ordered such that $\lambda_1 \geq \lambda_2 \geq \lambda_3$ and $\sum_i \lambda_i = 0$. The extraction of these

eigenvalues allows for the generation of an invariant map, also called the Lumley triangle, using the second and third principal components of turbulence anisotropy, defined as

$$II = a_{ij}a_{ji}/2 = \lambda_1^2 + \lambda_1\lambda_2 + \lambda_2^2, \quad (47)$$

$$III = a_{ij}a_{jn}a_{ni}/3 = -\lambda_1\lambda_2(\lambda_1 + \lambda_2), \quad (48)$$

where Einstein notation is used and repeated indices are summed. Another slight scaling based on these same invariants is referred to as the turbulence triangle, using the coordinates (η, ξ) where

$$\xi^3 = III/2, \quad (49)$$

$$\eta^2 = II/3. \quad (50)$$

As Emory notes, this mapping stretches the lower left quadrant of the Lumley triangle, providing more space to the region near the isotropic corner. These two triangles non-linearly map all possible turbulent states at a given point in space to a point within the triangle maps shown in Figure 42.

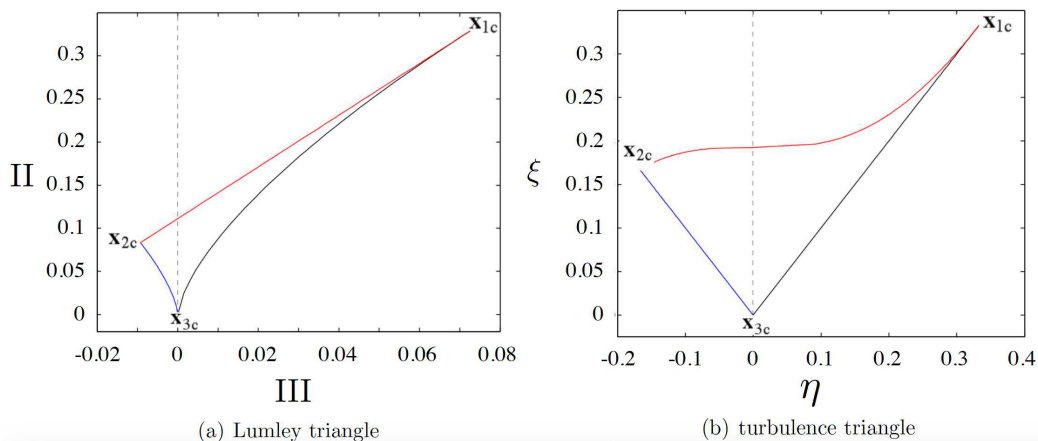


Figure 42: Diagram of the Lumley triangle and turbulence triangle non-linear anisotropy invariant maps. The limiting states of componentiality are label along with the plane-strain limit (dashed line) for reference [60].

There are three limiting states of componentiality for a turbulent field, which are:

1. one-component (x_{1C}) turbulence, where turbulent fluctuations only exist in a single direction. This has limiting eigenvalues $\lambda_1 = \frac{2}{3}$, $\lambda_2 = -\frac{1}{3}$, and $\lambda_3 = -\frac{1}{3}$. Turbulence in a single direction is also referred to as rod-like turbulence.
2. axisymmetric two-component (x_{2C}) turbulence, where turbulent fluctuations are equal in two directions. The limiting eigenvalues for this state are $\lambda_1 = \frac{1}{6}$, $\lambda_2 = \frac{1}{6}$, and $\lambda_3 = -\frac{1}{3}$. Axisymmetric two-component turbulence is also referred to as pancake-like turbulence.
3. isotropic (three-component, x_{3C}) turbulence, where turbulent fluctuations are equal in all three directions. The limiting eigenvalues for this state are $\lambda_1 = \lambda_2 = \lambda_3 = 0$.

These three limiting states are the triangular vertices shown in Figure 42. To visualize the anisotropy of turbulence seen in the numerical simulations presented here, the barycentric map of Banerjee [62] is constructed. This barycentric map functions based on the fact that any turbulence in a turbulent field is a convex combination of the three limiting states. Using these three limiting states as corners of an equilateral triangle, they are arbitrarily placed at $x_{1C} = (0, 0)$, $x_{2C} = (1, 0)$, and $x_{3C} = (1/2, \sqrt{3}/2)$ in a Euclidean domain.

The resulting coordinate system (x_B, y_B) is defined by

$$\begin{aligned} x_B &= C_{1C}x_{1C} + C_{2C}x_{2C} + C_{3C}x_{3C} = C_{1C} + \frac{1}{2}C_{3C} \\ y_B &= C_{1C}y_{1C} + C_{2C}y_{2C} + C_{3C}y_{3C} = \frac{\sqrt{3}}{2}C_{3C} \end{aligned}$$

with weights

$$C_{1C} = \lambda_1 - \lambda_2, \quad C_{2C} = 2(\lambda_2 - \lambda_3), \quad \text{and} \quad C_{3C} = \lambda_3 + 1.$$

Uniqueness for this system is enforced by $\sum_i C_{iC} = 1$. To generate an interesting figure to visualize large amounts of anisotropy data, a color scheme is developed. Here, there are three weights, which could easily correspond to the three colors, red, green, and blue to form an RGB triplet. Such an invariant map coloring can make it difficult to isolate regions that are close to one of the three limiting states, as most of the domain is somewhat similarly colored. To improve on this, Emory suggests alternative componentiality color contours that enhance the visual perception of the limiting states.

One such map gives a formulation for the RGB channel values as

$$\begin{bmatrix} R \\ G \\ B \end{bmatrix} = C_{1C}^* \begin{bmatrix} 0.5 \\ 0.5 \\ -0.5 \end{bmatrix} + C_{2C}^* \begin{bmatrix} 0.5 \\ -0.5 \\ 0.5 \end{bmatrix} + C_{3C}^* \begin{bmatrix} 0.5 \\ 0.5 \\ -0.5 \end{bmatrix} \quad (51)$$

where $C_{iC}^* = (C_{iC} + 1.75)^2$. Here, instead of using the red, green, and blue colors ($[1, 0, 0]^T$, $[0, 1, 0]^T$, and $[0, 0, 1]^T$, respectively), this colormap (equation 51) uses yellow, magenta, and cyan as a base. This mapping highlights each of the three limiting states clearly, giving the colormap for the barycentric triangle as seen in Figure 43.

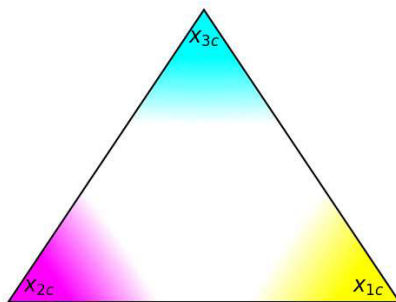


Figure 43: Barycentric anisotropic turbulence triangle colormap.

This colormap highlights rod-like turbulence in yellow, pancake-like turbulence in magenta, and isotropic turbulence in cyan, while leaving the remaining mixed-states as white. Figure 44 shows this colormap applied to the xy plane at $z/H = 0.30$. Figure 45 shows this colormap with contours for the energy loss coefficient ξ at different downstream yz planes. These figures show results for the no cavity case. The turbulence of this case is representative of the canonical flows seen in a turbine, and therefore illustrates the main results and advantages of this anisotropy analysis.

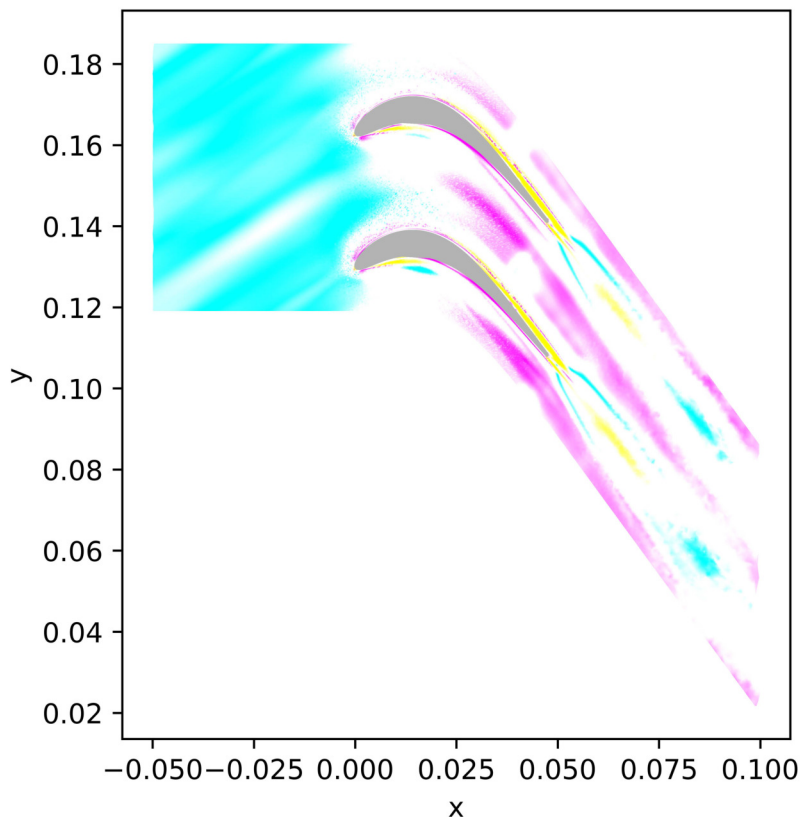


Figure 44: xy plane at $z/H = 0.3$ turbulence anisotropy.

Figure 44 shows that the incoming flow to the blades is isotropic, as the flow for $x < 0$ is cyan. This further supports that the turbulence injection method is working as expected. As the flow comes into contact with the blades, a few patterns emerge. In the separated region on the pressure sides of the blades, a noticeable yellow spot emerges, indicating single component turbulence. This rod-like turbulence is likely related to turbulence in the blade span direction. This rod-like turbulence also appears to break down over a short distance into more isotropic turbulence, as evidenced by the cyan spot just downstream. Over the blade surface, a magenta layer forms, indicating the development of two-component turbulence, as expected near a wall. This turbulence also appears to separate on the suction side of the blade, forming a yellow, one-component, turbulence region. Downstream of the trailing edge of the blades, two streaks of cyan appear where the trailing edge wake on average contributes to isotropic turbulence. Slightly further downstream of the trailing edge, a patch of one-component turbulence is seen which is

representative of the wake structures forming with turbulence in the spanwise direction. This then breaks down into isotropic turbulence.

One feature that Figure 44 captures is the stretching of vortical structures in the blade passage. The initially isotropic (cyan) flow enters the blade passage and turns to two-component turbulence (magenta), which is understandable since the acceleration of the flow in the passage direction should reduce turbulent fluctuations in this passage direction, leaving the two other turbulent fluctuations relatively unchanged.

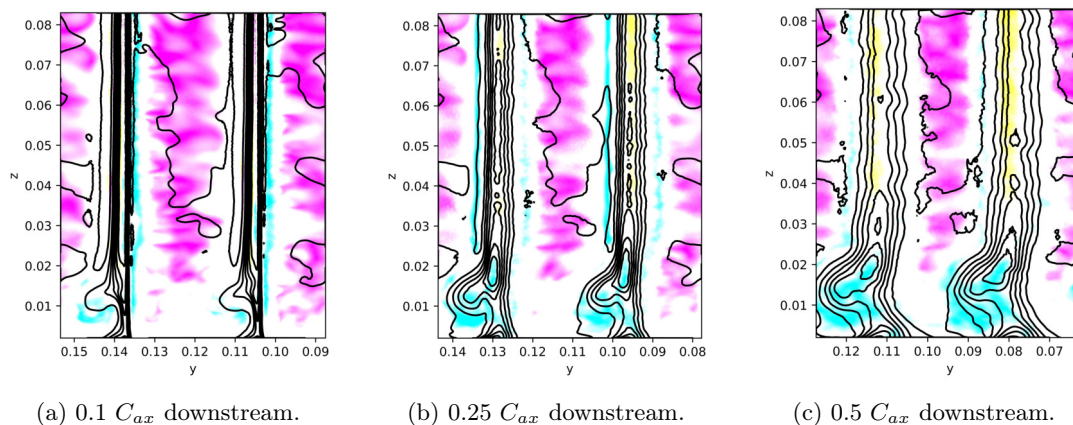


Figure 45: Turbulent anisotropy downstream evolution with ξ contours.

Figure 45 shows how the anisotropy of the turbulence in the flow evolves downstream of the blades, as well as how the contours of ξ vary downstream. Here, two main effects are observed. Firstly, the ξ contours widen downstream, indicating that mixing is occurring downstream of the wakes. Secondly, the isotropic turbulence region attributed to the passage vortex grows as well. The flow between the two blades, which was initially two-component (as seen in Figure 45a), becomes less two-component downstream. This also suggests strong mixing effects downstream of the blades, as expected.

Looking at Figure 45c shows the anisotropy of the turbulence at Plane 06 ($0.5 C_{ax}$ downstream), overlaid with contours of the energy loss coefficient, ξ . A few features are shared between the anisotropy shapes and the contours of the energy loss coefficient. For instance, the wakes are seen in yellow as rod like turbulence, and these wakes are similarly seen in the ξ contours. Additionally, the blade to blade passage far from the blades sees the two-component turbulence as discussed before, which also coincides with regions of reduced ξ . The passage vortex can be identified as the large cyan region at the bottom of the figure, and seems to coincide with regions of increased ξ .

Examining the turbulence anisotropy in the blade passage after the simulations reinforces the necessity of LES for these simulations; the variations and different turbulent structures seen are necessary to the accurate description of the flow physics.

4.4 Discussion

The simulated SPLEEN high-speed low-pressure turbine cascade produced results that follow the canonical flow shapes and correctly reproduced the known trends of the influence of the cavity and purge flow effects on the losses in the blade passage as seen experimentally [45].

In these simulations, the aspect that needs the most improvement is the angle of attack seen by the blades at Plane 02. The difference in the overall angle trend relative to experimentally seen results suggests that there are additional physics captured in the simulations that are not seen experimentally. Firstly, the very low angle of attack seen at the base of the blades (Figure 15) leads to separation at the bottom portion of the blades. This separation region may be affecting the flow attachment higher up in the blade span (e.g. $z/H = 0.3$), where the incoming angle is correct. This flow separation on the pressure side of the blades was also predicted by Okada [44] using a 2D steady RANS approach with a $k - \omega$ model with $\gamma - Re_\theta$ transition at the correct angle of attack. This suggests that even with the correct angle of attack the laminar to turbulent boundary layer transition taking place on the suction side of the blade is quite sensitive, and may require an extremely fine mesh in order to capture the turbulent scales that drive this transition. One method for improving on the angle of attack seen by the blades is a redesign of the computational domain such that the boundary layer trap is removed, and a slip wall is put in place between the inlet and the boundary layer trap tip. This has the downside of removing the effects of the boundary layer trap, however, which may have important effects on the development of the boundary layer at the hub.

Nonetheless, even with a large variation in the incoming angle of attack seen by the blades, the Plane 06 averaged loss coefficient ξ is well predicted, as seen in Figure 36. This suggests that the current simulations are reasonably accurately reproducing the vortex formation physics that are driving the mixing and subsequent loss mechanisms. The most notable difference in the loss coefficient is very close to the hub wall, which could be due to the way the boundary layer on the hub wall develops from the beginning at the hub tip and boundary layer trap interface.

From these results, it is clear that the inclusion of the cavity (even without purge mass flow) directly affects the horseshoe vortex formation at the blade leading edge. This disruption in the vortex formation leads to an intensification of the blade passage vortex, which then leads to more losses as this vortex is accelerated through the blade passage and then mixed with other secondary flows after the blades. With purge mass flow, this intensification is even stronger, as the purge flow bends due to the potential effect of the blades and combines with the passage vortex.

Examining the turbulence anisotropy in the blade passage after the simulations reinforces the necessity of LES for these simulations; the variations and different turbulent structures seen are necessary to the accurate description of the flow physics. These turbulent structures seem to be linked to loss mechanisms seen in the flow. More specifically, it appears as though the breakdown from one- or two-dimensional turbulence towards isotropic turbulence leads to the generation of losses. However, this breakdown process may be relatively unimportant compared to the mixing/bursting of large vortical structures, and further investigation is needed to relate the anisotropy of the flow to the losses.

5 Conclusion

This simulation endeavor balanced computational cost and complexity, employing state of the art large eddy simulation for a turbine cascade operating at high-speed low-pressure conditions necessary for future improvements to turbomachines. Overall, this project cost more than 870 thousand hours on the Centre de Calcul Recherche et Technologie (CCRT) supercomputer TOPAZE, generating over 4Tb of data. Such complex CFD projects are limited almost exclusively to research and academic domains and help to build a deeper understanding of relevant physics in order to construct better models in the future. Here, the SPLEEN simulations performed provide valuable insight as to how to better model these turbine cascades in the future.

As engine designs evolve, being able to simulate the design while including a range of technological effects will continue to present a significant challenge. This project demonstrated that AVBP is able to model a high-speed low-pressure turbine with turbulence injection and include purge flow effects. Overall, this simulation is the culmination of a variety of mathematical techniques, advanced modeling, turbulence injection methods, and numerical post-treatments applied to a complex problem with an experimental reference. The development of this project uncovered a few discrepancies in the AVBP source code, which were corrected to produce a more robust, accurate turbulence injection method. Lastly, a newer method for inspecting the anisotropy of turbulence in the domain was employed, which recovered relevant results for describing loss generation.

The current simulations have shown good agreement with experimentally available values, and have also uncovered some of the central issues with numerically recreating these test setups. In depth analysis on the flow fields revealed how the cavity influences the development of losses in the turbine cascade, and has highlighted the importance of these technological features as the need for accurate design and modeling increases.

6 Perspectives

Throughout this project, the two main challenges were: to inject the correct turbulence, and to match the experimental operating point. The turbulence injected here matches the correct turbulence intensity and the integral length scale, after the bug corrections. Accurately modeling the turbulence was the main driver of the cost of the simulation as increasing the refinement of the mesh between the inlet and the blades directly drives the minimum resolved turbulence size. Unfortunately, this section of the domain was also extremely large, and potential effects from the boundary layer trap or hub boundary layer development may require the inlet to be even further from the blades, which would greatly increase the cost of the simulation. Instead, an alternative simulation method might focus on characterizing the rms values of the flow and the mean flow profile at a pseudo-inlet plane at some point past the hub tip. This could allow for an accurate characterization of the turbulence and mean profiles and their effects on the blades while reducing the cost. Matching the experimental operating point proved to be quite difficult, especially as it relates to the angle of attack that reaches the blades. Changing to this inlet plane might allow for the angle of attack to be numerically imposed the same as the experiment with the correct turbulence statistics.

Further work on this project would include the rotating bars to complete the numerical simulation of the experimental set up. This can be accomplished in AVBP using methods for coupling multiple simulations and overlapping their meshes so that information can be transmitted between static and rotating (or sliding) components. Adding these components would greatly increase the complexity of the simulation and would likely require an even finer mesh to accurately describe the fine wakes generated from the 1 mm moving rods.

A Turbulent Injection Methods, Detailed

Some of the material covered in Section 4.2.2 will be repeated here, but with additional explanation.

The goal of the turbulence injection is to apply perturbations to the inlet velocity profile to generate divergence-free, statistically stationary turbulence with user defined statistics. In these simulations, this is accomplished by constructing a velocity perturbation field, $\Delta \mathbf{u}(x, t)$, such that the inlet velocity is $\mathbf{u}(\mathbf{x}, t) = \bar{\mathbf{u}}(\mathbf{x}) + \mathbf{u}'(\mathbf{x}, t)$, employing Taylor's assumption. This velocity perturbation field is largely based on the work from Kraichnan [50], and extended with Bailly's method [63].

A.1 Kraichnan's Method

Kraichnan's method was initially implemented in AVBP by Guézennec [64]. Kraichnan generates an initial velocity perturbation field using randomly sampled Fourier harmonics, which results in a divergence-free, statistically stationary, homogeneous, isotropic turbulent perturbation. Firstly, the relation between the fluctuating velocity field $\mathbf{u}'(\mathbf{x}, t)$ and its three-dimensional Fourier transform in the space $\hat{\mathbf{u}}(\mathbf{k}, t)$ at the wave vector \mathbf{k} is:

$$\mathbf{u}'(\mathbf{x}, t) = \int_D \hat{\mathbf{u}}(\mathbf{k}, t) e^{i\mathbf{k}\mathbf{x}} d^3\mathbf{x} \quad (\text{A.1})$$

where D indicates the domain of \mathbf{k} . As the Taylor assumption is applied,

$$\hat{\mathbf{u}}(\mathbf{k}, t) = \hat{\mathbf{u}}(\mathbf{k}) e^{i\omega t}, \quad \omega = \mathbf{k} \cdot \bar{\mathbf{u}}. \quad (\text{A.2})$$

Thus, equation A.1 becomes:

$$\mathbf{u}'(\mathbf{x}, t) = \int_D \hat{\mathbf{u}}(\mathbf{k}) e^{i(\mathbf{k}\mathbf{x} - \omega t)} d^3\mathbf{x}, \quad (\text{A.3})$$

using $i = \sqrt{-1}$. When the fluctuating velocity field is assumed to be incompressible, $\nabla \mathbf{u}' = 0$. This property is expressed in the spectral domain as:

$$\hat{\mathbf{u}}(\mathbf{k}) \cdot \mathbf{k} = 0, \quad (\text{A.4})$$

which shows that $\hat{\mathbf{u}}(\mathbf{k})$ is perpendicular to the wave vector, \mathbf{k} . Equation A.3 must be approximated with N modes, which gives:

$$\mathbf{u}'(\mathbf{x}, t) = \sum_{n=1}^N \hat{\mathbf{u}}_{\mathbf{n}}(\mathbf{k}_n) e^{i(\mathbf{k}_n \mathbf{x} - \omega_n t)}, \quad (\text{A.5})$$

$$\hat{\mathbf{u}}_{\mathbf{n}} \cdot \mathbf{k}_n = 0 \quad \forall n.$$

Here, $\hat{\mathbf{u}}_{\mathbf{n}}(\mathbf{k}_n)$ is the discrete three-dimensional Fourier transform of the fluctuating velocity field at the wave vector \mathbf{k}_n with $\omega_n = \mathbf{k}_n \cdot \bar{\mathbf{u}}$ as the pulsation. As \mathbf{u}' is real in the physical space, it is equal to its complex conjugate, \mathbf{u}'^* , which also holds for its Fourier transform. Thus,

$$\mathbf{u}'^*(\mathbf{x}, t) = \sum_{n=1}^N \hat{\mathbf{u}}_{\mathbf{n}}(\mathbf{k}_n) e^{-i(\mathbf{k}_n \mathbf{x} + \omega_n t)}, \quad (\text{A.6})$$

Summing equations A.5 and A.6 allows the equation for the perturbation velocity to be rewritten in terms of sines and cosines as:

$$\mathbf{u}'(\mathbf{x}, t) = \sum_{n=1}^N [\hat{\mathbf{v}}_n(\mathbf{k}_n) \cos(\mathbf{k}_n \cdot \mathbf{x} + \omega_n t) + \hat{\mathbf{w}}_n(\mathbf{k}_n) \sin(\mathbf{k}_n \cdot \mathbf{x} + \omega_n t)], \quad (\text{A.7})$$

where $\hat{\mathbf{v}}_n = \Re(\hat{\mathbf{u}}_n(\mathbf{k}_n))$ and $\hat{\mathbf{w}}_n = \Im(\hat{\mathbf{u}}_n(\mathbf{k}_n))$, and

$$\hat{\mathbf{v}}_n \cdot \mathbf{k}_n = 0 \quad \text{and} \quad \hat{\mathbf{w}}_n \cdot \mathbf{k}_n = 0 \quad \forall n. \quad (\text{A.8})$$

As Guézennec [64] states, the last step before the implementation of the Kraichnan method is to convert the previous system to dimensionless quantities. To perform this nondimensionalization, the characteristic quantities are the turbulent velocity, $|\mathbf{u}_p|$, the most energetic wave length of the turbulent spectrum, λ_e its corresponding time-scale, $\tau_e = \frac{\lambda_e}{|\bar{\mathbf{u}}|}$.

With these characteristic quantities, the resulting dimensionless equation is written as

$$\tilde{\mathbf{u}}'(\tilde{\mathbf{x}}, t) = \sum_{n=1}^N \left[\hat{\tilde{\mathbf{v}}}_n(\tilde{\mathbf{k}}_n) \cos(\tilde{\mathbf{k}}_n \cdot \tilde{\mathbf{x}} + \tilde{\omega}_n t) + \hat{\tilde{\mathbf{w}}}_n(\tilde{\mathbf{k}}_n) \sin(\tilde{\mathbf{k}}_n \cdot \tilde{\mathbf{x}} + \tilde{\omega}_n t) \right] \quad (\text{A.9})$$

$$\hat{\tilde{\mathbf{v}}}_n \cdot \tilde{\mathbf{k}}_n = 0 \quad \text{and} \quad \hat{\tilde{\mathbf{w}}}_n \cdot \tilde{\mathbf{k}}_n = 0 \quad \forall n. \quad (\text{A.10})$$

where the $\tilde{\cdot}$ indicates a dimensionless quantity. To simplify the notation, the $\tilde{\cdot}$ symbol will be suppressed and quantities will be implicitly dimensionless.

Kraichnan generates, for all N , two real vectors $\hat{\mathbf{v}}_n$ and $\hat{\mathbf{w}}_n$ such that the injected flow is incompressible (Equation A.10) and the desired turbulent spectrum $E(k)$ is recovered. To do so, the vectors $\hat{\mathbf{v}}_n$ and $\hat{\mathbf{w}}_n$ are chosen as follows:

$$\hat{\mathbf{v}}_n = \zeta_n \times \mathbf{k}_n \quad \text{and} \quad \hat{\mathbf{w}}_n = \eta_n \times \mathbf{k}_n \quad \forall n. \quad (\text{A.11})$$

The vectors ζ_n and η_n are independently picked from a three-dimensional Gaussian distribution, with standard deviation $\sigma_N = \sqrt{\frac{2}{N}}$. This value is chosen such that $\overline{u'_i u'_i} = 1$.

To generate the wave vectors \mathbf{k}_n and the pulsations ω_n , these are chosen from statistically isotropic distributions shaped such that the desired turbulent spectrum $E(k)$ would be recovered in the limit $N \rightarrow \infty$. Kraichnan recovers the Passot-Pouquet spectrum by picking the components for \mathbf{k}_n and ω_n randomly from Gaussian distributions with a standard deviation $\sigma = \frac{1}{2}$.

A.2 Bailly's Method

Bailly's method takes a very similar approach to Kraichnan's but extends this method to allow for other turbulent spectrums to be recovered, and also allows for a variable energetic length scale to be injected.

Bailly considers the three-dimensional Fourier transform in space of the instantaneous velocity field \mathbf{u}' . A straightforward geometrical argument can be made to adjust $\hat{\mathbf{v}}_n = \hat{\mathbf{u}}_a$ and $\hat{\mathbf{w}}_n = \hat{\mathbf{u}}_b$, based on Figure 46.

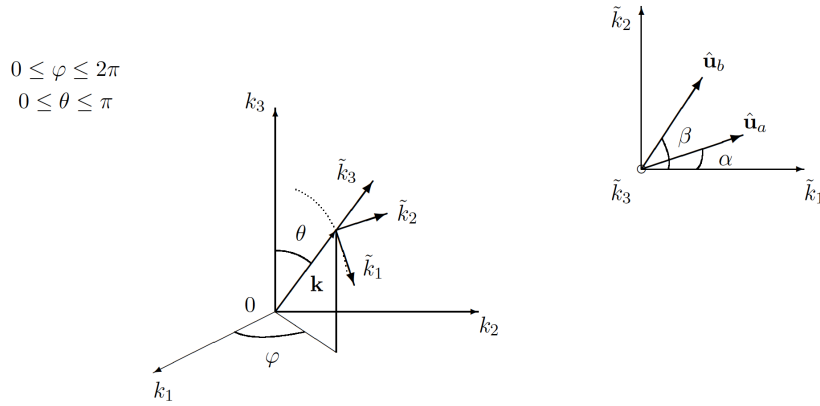


Figure 46: Local frame $(\tilde{k}_1, \tilde{k}_2, \tilde{k}_3)$ in \mathbf{k} space corresponding to $(e_\theta, e_\varphi, e_r)$ in spherical coordinates, and representation of the Fourier component $\hat{\mathbf{u}}(\mathbf{k}) = \hat{\mathbf{u}}_a - \nu \hat{\mathbf{u}}_b$ [63].

Bailly notes that since these two vectors are perpendicular to \mathbf{k}_n , in the local frame aligned with \mathbf{k}_n the coordinates of these two vectors can be written as

$$\hat{\mathbf{v}}_n = \hat{\mathbf{u}}_a = \hat{u} \mathbf{a} = \hat{u} \begin{bmatrix} \cos \alpha \\ \sin \alpha \end{bmatrix} \quad \text{and} \quad \hat{\mathbf{w}}_n = \hat{\mathbf{u}}_b = \hat{u} \mathbf{b} = \hat{u} \begin{bmatrix} \cos \beta \\ \sin \beta \end{bmatrix}. \quad (\text{A.12})$$

Writing the velocity perturbation field as a Fourier series gives:

$$\mathbf{u}'(\mathbf{x}) = \sum_{n=1}^N [\hat{u}_n(\mathbf{k}_n) \cos(\mathbf{k}_n \cdot \mathbf{x}) \mathbf{a}_n + \hat{u}_n(\mathbf{k}_n) \sin(\mathbf{k}_n \cdot \mathbf{x}) \mathbf{b}_n]. \quad (\text{A.13})$$

A single realization of the isotropic turbulent field is then chosen by adding a phase shift of ψ_n to each of the modes, giving

$$\mathbf{u}'(\mathbf{x}) = \sum_{n=1}^N [\hat{u}_n(\mathbf{k}_n) \cos(\mathbf{k}_n \cdot \mathbf{x} + \psi_n) \mathbf{a}_n + \hat{u}_n(\mathbf{k}_n) \sin(\mathbf{k}_n \cdot \mathbf{x} + \psi_n) \mathbf{b}_n], \quad (\text{A.14})$$

and the variables ψ_n , \mathbf{k}_n , \mathbf{a}_n , and \mathbf{b}_n are taken to be random variables with given probability density functions. However, the corresponding amplitude of the n th mode \hat{u}_n is not chosen at random, and instead is chosen based on the turbulent kinetic energy spectrum, as will be shown later.

To enforce isotropy of the injected turbulence, the wave vector \mathbf{k}_n is picked randomly on a sphere, S , of radius k . In the Cartesian frame, the unit vectors of the local frame are:

$$\tilde{\mathbf{k}}_1 = \begin{bmatrix} \cos \theta \cos \varphi \\ \cos \theta \sin \varphi \\ -\sin \theta \end{bmatrix}, \quad \tilde{\mathbf{k}}_2 = \begin{bmatrix} -\sin \varphi \\ \cos \varphi \\ 0 \end{bmatrix}, \quad \text{and} \quad \tilde{\mathbf{k}}_3 = \begin{bmatrix} \sin \theta \cos \varphi \\ \sin \theta \sin \varphi \\ \cos \theta \end{bmatrix} \quad (\text{A.15})$$

yielding for $\mathbf{k} = k\tilde{\mathbf{k}}_3$:

$$\mathbf{k} = k \begin{bmatrix} \sin \theta \cos \varphi \\ \sin \theta \sin \varphi \\ \cos \theta \end{bmatrix} \quad (\text{A.16})$$

where $0 \leq \varphi \leq 2\phi$ and $0 \leq \theta \leq \pi$, as seen in Figure 46. On the sphere, S , the isotropy condition requires that

$$\frac{dS}{4\pi k^2} = \frac{k \sin \theta d\varphi k d\theta}{4\pi k^2} = p(\theta) d\theta p(\varphi) d\varphi. \quad (\text{A.17})$$

Equation A.17 above relates the probability of selecting a point on an infinitesimal part of the sphere's surface is equal to the probability density functions of the two random variables, θ and φ . Correspondingly, the probability density functions $p(\theta)$ and $p(\varphi)$ are taken by Bailly to be $p(\theta) = \sin(\theta)/2$ and $p(\varphi) = 1/(2\pi)$. The two unit vectors \mathbf{a} and \mathbf{b} introduced in Equation A.12 have an arbitrary orientation in their plane defined by $(\tilde{k}_1, \tilde{k}_2)$, where in Cartesian coordinates

$$\mathbf{a} = \begin{bmatrix} \cos \alpha \cos \theta \cos \varphi - \sin \alpha \sin \varphi \\ \cos \alpha \cos \theta \sin \varphi + \sin \alpha \sin \varphi \\ -\cos \alpha \sin \theta \end{bmatrix} \quad (\text{A.18})$$

and the same expression is obtained for \mathbf{b} , substituting β for α . Since the orientation of \mathbf{a} and \mathbf{b} are arbitrary, the random variables α and β are distributed uniformly between 0 and 2π , giving $p(\alpha) = p(\beta) = 1/(2\pi)$.

The final random variable is ψ_n , which relates to the phase of the mode. This is done by introducing the two-point correlation function of the velocity field:

$$R_{ij} = \overline{u'_i(\mathbf{x})u'_j(\mathbf{y})} \quad (\text{A.19})$$

where $\mathbf{y} = \mathbf{x} + \mathbf{d}$, with \mathbf{d} as an arbitrary vector separating the two points, \mathbf{x} and \mathbf{y} . The correlation function between these two points is obtained by taking the ensemble average of the following:

$$\begin{aligned} & \sum_n \hat{u}_n [\cos(\mathbf{k}_n \cdot \mathbf{x} + \psi_n) a_{ni} + \sin(\mathbf{k}_n \cdot \mathbf{x} + \psi_n) b_{ni}] \\ & \times \sum_m \hat{u}_m [\cos(\mathbf{k}_m \cdot \mathbf{y} + \psi_m) a_{mj} + \sin(\mathbf{k}_m \cdot \mathbf{y} + \psi_m) b_{mj}] \end{aligned}$$

As the N modes are statistically independent, and the two vectors \mathbf{a}_n and \mathbf{b}_n of the same n th mode are also independent, the expression can be reduced to:

$$\sum_n \hat{u}_n^2 [\cos(\mathbf{k}_n \cdot \mathbf{x} + \psi_n) \cos(\mathbf{k}_n \cdot \mathbf{y} + \psi_n) a_{ni} a_{nj} + \sin(\mathbf{k}_n \cdot \mathbf{x} + \psi_n) \sin(\mathbf{k}_n \cdot \mathbf{y} + \psi_n) b_{ni} b_{nj}].$$

Taking the ensemble average of this expression and recovering the correlation function, it yields:

$$\begin{aligned} \overline{u'_i(\mathbf{x})u'_j(\mathbf{x} + \mathbf{d})} &= \frac{1}{2} \sum_n \hat{u}_n^2 \left[\overline{\cos(\mathbf{k}_n \cdot \mathbf{d}) a_{ni} a_{nj}} + \overline{\cos(2\mathbf{k}_n \cdot \mathbf{x} + \mathbf{k}_n \cdot \mathbf{d} + 2\psi_n) a_{ni} a_{nj}} \right] \\ &+ \frac{1}{2} \sum_n \hat{u}_n^2 \left[\overline{\cos(\mathbf{k}_n \cdot \mathbf{d}) b_{ni} b_{nj}} - \overline{\cos(2\mathbf{k}_n \cdot \mathbf{x} + \mathbf{k}_n \cdot \mathbf{d} + 2\psi_n) b_{ni} b_{nj}} \right] \end{aligned} \quad (\text{A.20})$$

where $\bar{\cdot}$ is the ensemble average. In order to obtain a homogeneous velocity field such that $R_{ij} = R_{ij}(\mathbf{d})$ only, the random variable ψ_n must be uniformly distributed between 0 and 2π . This distribution reduces the expression further, yielding:

$$\begin{aligned}
R_{ij}(\mathbf{d}) &= \overline{u'_i(\mathbf{x})u'_j(\mathbf{x} + \mathbf{d})} \\
&= \frac{1}{2} \sum_{n=1}^N \hat{u}_n^2 \left[\overline{\cos(\mathbf{k}_n \cdot \mathbf{d})a_{ni}a_{nj}} + \overline{\cos(\mathbf{k}_n \cdot \mathbf{d})b_{ni}b_{nj}} \right], \tag{A.21}
\end{aligned}$$

where $\bar{\cdot} \equiv \langle \cdot \rangle_{\varphi, \theta, \alpha, \beta}$. Using this equation to evaluate the autocorrelation (i.e. $\mathbf{d} = 0$, $i = j$) at a given point, the turbulent kinetic energy (TKE) can be recovered as:

$$TKE = \frac{\overline{u'_i u'_i}}{2} = \frac{1}{2} R_{ii}(\mathbf{0}) = \frac{1}{2} \left(\frac{1}{2} \sum_{n=1}^N \hat{u}_n^2 [1 + 1] \right) = \frac{1}{2} \sum_{n=1}^N \hat{u}_n^2 \tag{A.22}$$

since \mathbf{a}_n and \mathbf{b}_n are unit vectors. Bailly then determines that for a given turbulent kinetic energy spectrum, $E(k)$, the amplitude of the n th Fourier mode can be calculated by

$$\hat{u}_n = \sqrt{2E(k_n)\Delta k_n} \tag{A.23}$$

where Δk_n is the step of the discretization in the Fourier space.

The Passot-Pouquet spectrum in Bailly's method is constructed via:

$$E(k) = A \left(\frac{k}{k_e} \right)^4 \exp \left[-2 \left(\frac{k}{k_e} \right)^2 \right] \tag{A.24}$$

with A as the amplitude of the spectrum and k_e is the wave number associated to the most energetic length scale. Lepage [48] shows that by defining the turbulent kinetic energy as $k \equiv \frac{1}{2} \overline{u'_i u'_i} = \frac{3}{2} U_p^2$ gives the constant A as:

$$A = \frac{16U_p^2}{k_e} \sqrt{\frac{2}{\pi}}. \tag{A.25}$$

The spectrum is defined for all wave numbers k with two factors, U_p and k_e . U_p controls the amplitude of the energy spectrum, and corresponds to the rms fluctuation of the velocity (assuming isotropic turbulence). This parameter is user-controlled to reach target turbulence intensity levels. k_e controls the position of the peak of the spectrum and its extent, and is related to the integral length scale, L_i , by:

$$L_i = \frac{\sqrt{2\pi}}{k_e}. \tag{A.26}$$

Within AVBP, the wave numbers, k , are generated based on the user input number of modes, N , as

$$k_j = \exp \left[\ln(k_{min}) + (\ln(k_c) - \ln(k_{min})) * \frac{j-1}{N-1} \right], \quad j = 1, \dots, N. \tag{A.27}$$

This method also determines the discretization size, Δk , needed to calculate the magnitude of the n th mode, as shown in Equation A.23. Here, k_{min} is determined based off the maximum turbulent length, L_{max} injected as

$$k_{min} = \frac{2\pi}{L_{max}}. \tag{A.28}$$

Likewise, the cutoff wave number, k_c , is determined based off the user input cutoff length as

$$k_c = \frac{2\pi}{L_c}. \quad (\text{A.29})$$

Periodicity for Bailly’s injection method is achieved by rescaling the wavevector in the periodic direction by an appropriate ratio. Recall from Equation A.16 that the wavevector \mathbf{k} is a randomly-directed vector with length k , and from Equation A.14 it is clear that the wavevector \mathbf{k} adjusts the shapes of the Fourier modes used to perturb the inlet. To force periodicity, these N modes are rescaled in the appropriate i th direction by

$$k_{n,i} = k_{n,i} \frac{2\pi}{l_i} \quad (\text{A.30})$$

where l_i is the periodic length in the i th direction. With this scaling, it is clear that the product $k_{n,i}x_i$ in the cosine or sine term in Equation A.14 is scaled to be in the range $[0, 2\pi]$, ensuring that the two sides of the domain are equal. In the actual numerical implementation, this periodicity can be susceptible to drift, as the periodicity is enforced by construction but not numerically. To prevent this drift, these simulations also enforced periodicity by equating the density, the density times the velocity, and the density times the total energy on periodic nodes every 1000 iterations. These periodic corrections were typically very small; for example, the maximum correction over all nodes for the density at the inlet for a representative 1000 iterations was 1.93×10^{-4} kg/m³. With an inlet density of 0.097 kg/m³, this corresponds to a correction of less than one percent, which is on the same order as the other corrections.

B Bug Correction for Turbulent Injection Methods

While the implementation of Bailly’s method was correct for the majority of cases, this simulation presented an unusual situation where the flow was entering the domain at an angle. This angle in the mesh and in AVBP included a z component in the default frame of reference, which lead to one significant bug. During this bugfixing, another smaller bug was also uncovered.

To explain how this bug was discovered it is useful to discuss AVBP’s code flowchart for implementing turbulence. Firstly, AVBP reads the inlet boundary condition type (in this case, INLET_RELAX_PT_TT_Y_TURB) and determines the current state of the inlet. Since the keyword "_TURB" is included, the turbulent perturbation is determined via a call to `inlet_turb.f90`. This wrapper function handles the majority of the parameters and handles the calls to other subfunctions to generate the turbulent perturbations.

The key subfunction that computes these turbulent perturbations is `set_turb_modes.f90`, which follows the procedures to generate the Fourier modes as described by Bailly (or Kraichnan for other methods of injection). The minor bug uncovered in this function relates to the vectors \mathbf{a} and \mathbf{b} , the unit vectors used to define the plane perpendicular to the wavevector, \mathbf{k} . As Equation A.18 indicates, the first component (in the x direction) should be determined by

$$a_x = \cos \alpha \cos \theta \cos \varphi - \sin \alpha \sin \varphi.$$

The subfunction `set_turb_modes.f90` has a mistake in the sign between these two terms, for both a_x and b_x (line 279, 283 in AVBP 7.12). This incorrect sign violates an important property of these vectors, since the magnitude of either \mathbf{a} or \mathbf{b} are not guaranteed to be one, as expected. This also has implications for the generation of turbulent perturbation, as each of the modes are scaled by these vectors. The improper generation of these vectors likely leads to the generation of a anisotropic turbulence, even in the case that the user requests such a field. This error is less severe than the other bug discovered, however.

The other bug discovered comes after the call to `set_turb_modes.f90`, where `inlet_turb.f90` then calls `set_turb_pert_old.f90` to apply these modes to generate the actual velocity perturbation. The perturbation is calculated in AVBP as

$$\mathbf{u}'(\mathbf{x}) = c_1 \cos \mathcal{A} + c_2 \sin \mathcal{A} + \frac{\partial \mathcal{A}}{\partial t} (-c_1 \sin \mathcal{A} + c_2 \cos \mathcal{A}), \quad (\text{B.1})$$

where the coefficients $c_1 = \hat{u}_n(\mathbf{k}_n) \mathbf{a}_n$, $c_2 = \hat{u}_n(\mathbf{k}_n) \mathbf{b}_n$, and the argument of the cosine or sine term, $\mathcal{A} = \mathbf{k}_n \cdot \mathbf{x} + \psi_n + \omega_n t$. This is a straightforward application of a first order Taylor expansion.

The code generates a 2D section of perturbations located at $\mathbf{u}_{c,p} t$ upstream of the inlet section (where $\mathbf{u}_{c,p}$ is the convective velocity perpendicular to the inlet). The term $+\omega_n t$ is computed by $-\mathbf{k}_{n,p} \mathbf{u}_{c,p} t$, where $\mathbf{k}_{n,p}$ is the perpendicular mode to the inlet plane. This change in sign was not correctly implemented in the z direction, initially having a contribution to the time derivative term as

$$\frac{\partial \mathcal{A}_z}{\partial t} = k_{z,n} u_{c,z} \quad (\text{B.2})$$

instead of the correct contribution,

$$\frac{\partial \mathcal{A}_z}{\partial t} = -k_{z,n} u_{c,z}. \quad (\text{B.3})$$

Of course, this incorrect sign is only significant when there is a convective velocity in the z direction, as otherwise this term's sign error would be zeroed out. For instance, if the flow enters only in the x direction, $u_{c,z} = 0$ and the sign error will not be apparent. This bug is severe in the case where $u_{c,z} \neq 0$, as the resulting velocity perturbations are completely incorrect, and resulted in turbulence values that were much greater than expected (an order of magnitude higher at points).

References

- [1] J. Kurzke. Fundamental Differences Between Conventional and Geared Turbofans. volume Volume 1: Aircraft Engine; Ceramics; Coal, Biomass and Alternative Fuels; Controls, Diagnostics and Instrumentation; Education; Electric Power; Awards and Honors of *Turbo Expo: Power for Land, Sea, and Air*, pages 145–153, June 2009.
- [2] B. K. Kestner, J. S. Schutte, J. C. Gladin, and D. N. Mavris. Ultra High Bypass Ratio Engine Sizing and Cycle Selection Study for a Subsonic Commercial Aircraft in the N+2 Timeframe. volume Volume 1: Aircraft Engine; Ceramics; Coal, Biomass and Alternative Fuels; Wind Turbine Technology of *Turbo Expo: Power for Land, Sea, and Air*, pages 127–137, June 2011.
- [3] M. Giovannini, F. Rubecchini, M. Marconcini, A. Arnone, and F. Bertini. Analysis of a LPT Rotor Blade for a Geared Engine: Part I — Aero-Mechanical Design and Validation. volume Volume 2B: Turbomachinery of *Turbo Expo: Power for Land, Sea, and Air*, June 2016. V02BT38A053.
- [4] G. Pastorino, L. Simonassi, G. Lopes, E. Boufidi, F. Fontaneto, and S. Lavagnoli. Measurements of Turbulence in compressible Low-Density Flows at the Inlet of a Transonic Linear Cascade with and without Unsteady Wakes. volume Proceedings of ASME Turbo Expo 2023 of *Turbomachinery Technical Conference and Exposition*, June 2023. GT2023-103712.
- [5] L. Stein. *A Skew-Symmetric, Conservative Finite Difference Scheme for the Simulation of Reactive Flow*. PhD thesis, March 2013.
- [6] S. Goto. A physical mechanism of the energy cascade in homogeneous isotropic turbulence. *Journal of Fluid Mechanics*, 605, 2008.
- [7] A. N. Kolmogorov. A refinement of previous hypotheses concerning the local structure of turbulence in a viscous incompressible fluid at high reynolds number. *Journal of Fluid Mechanics*, 13(1):82–85, 1962.
- [8] P.E. Roach. The generation of nearly isotropic turbulence by means of grids. *International Journal of Heat and Fluid Flow*, 8(2):82–92, 1987.
- [9] A. Trush, S. Pospíšil, and H. Kozmar. Comparison of turbulence integral length scale determination methods. *WIT Transactions on Engineering Sciences*, 128:113–123, 2020.
- [10] S. Pope. Stochastic lagrangian models of velocity in homogeneous turbulent shear flow. *Physics of fluids*, 14(5):1696–1702, 2002.
- [11] A. Leonard. Energy cascade in large eddy simulations of turbulent fluid flow. *Adv. Geophys.*, 18A:237–248, January 1974.
- [12] J. Smagorinsky. General circulation experiments with the primitive equations: I. the basic experiment. *Monthly Weather Review*, 91(3):99 – 164, 1963.
- [13] M. Germano, U. Piomelli, P. Moin, and W. Cabot. A dynamic subgrid-scale eddy viscosity model. *Physics of Fluids A: Fluid Dynamics*, 3(7):1760–1765, 1991.
- [14] F. Nicoud and F. Ducros. Subgrid-scale stress modelling based on the square of the velocity gradient tensor. *Flow, Turbulence and Combustion*, 62(3):183–200, 1999.

- [15] N. Franck, H. Toda, O. Cabrit, S. Bose, and J. Lee. Using singular values to build a subgrid-scale model for large eddy simulation. *Physics of Fluids - PHYS FLUIDS*, 23, August 2011.
- [16] L. M. S. Troth. *Multiphysics coupled simulations of gas turbines*. Phd thesis, Institut National Polytechnique de Toulouse, November 2017.
- [17] T. Léonard, L. Gicquel, N. Gourdain, and F. Duchaine. Steady/Unsteady Reynolds-Averaged Navier–Stokes and Large Eddy Simulations of a Turbine Blade at High Subsonic Outlet Mach Number. *Journal of Turbomachinery*, 137(4), October 2014. 041001.
- [18] K. W. Morton, P. I. Crumpton, and J. A. Mackenzie. Cell vertex methods for inviscid and viscous flows. *Computers & Fluids*, 22(2):91–102, 1993.
- [19] T. Schonfeld and M. Rudgyard. Steady and unsteady flow simulations using the hybrid flow solver avbp. *AIAA Journal*, 37(11):1378–1385, 1999.
- [20] T. Poinso. Boundary conditions for direct simulations of compressible viscous flows. *Journal of Computational Physics*, 101:104–129, 1992.
- [21] N. Guezennec and T. Poinso. Acoustically nonreflecting and reflecting boundary conditions for vorticity injection in compressible solvers. *AIAA Journal*, 47(7):1709–1722, 2009.
- [22] N. Odier, M. Sanjosé, L. Gicquel, T. Poinso, S. Moreau, and F. Duchaine. A characteristic inlet boundary condition for compressible, turbulent, multispecies turbomachinery flows. *Computers & Fluids*, 178:41–55, 2019.
- [23] V. Granet, O. Vermorel, T. Léonard, L. Gicquel, and T. Poinso. Comparison of nonreflecting outlet boundary conditions for compressible solvers on unstructured grids. *AIAA Journal*, 48(10):2348–2364, 2010.
- [24] P. Lax and B. Wendroff. Systems of conservation laws. *Communications on Pure and Applied Mathematics*, 13(2):217–237, 1960.
- [25] O. Colin and M. Rudgyard. Development of high-order taylor–galerkin schemes for les. *Journal of Computational Physics*, 162(2):338–371, 2000.
- [26] A. Misdariis, A. Robert, O. Vermorel, S. Richard, and T. Poinso. Numerical Methods and Turbulence Modeling for LES of Piston Engines: Impact on Flow Motion and Combustion. *Oil & Gas Science and Technology - Revue d'IFP Energies nouvelles*, 69(1):83–105, February 2013.
- [27] Colin, O., Benkenida, A., and Angelberger, C. 3d modeling of mixing, ignition and combustion phenomena in highly stratified gasoline engines. *Oil & Gas Science and Technology - Rev. IFP*, 58(1):47–62, 2003.
- [28] R. H. Ni. *A multiple grid scheme for solving the Euler equations*. Number 0 in Fluid Dynamics and Co-located Conferences. American Institute of Aeronautics and Astronautics, 2023/09/04 1981.
- [29] S. Dellacherie. Checkerboard modes and wave equation. In *Proceedings of Algorithmy*, volume 2009, pages 71–80, 2009.
- [30] M. Malandain. *Simulation massivement parallèle des écoulements turbulents à faible nombre de Mach*. Theses, INSA de Rouen, January 2013.

- [31] N. A. Cumpsty and J. H. Horlock. Averaging Non-Uniform Flow for a Purpose. volume Volume 6: Turbo Expo 2005, Parts A and B of *Turbo Expo: Power for Land, Sea, and Air*, pages 1–14, June 2005.
- [32] D. Giesecke, M. Lehmler, J. Friedrichs, J. Blinstrub, L. Bertsch, and W. Heinze. Evaluation of ultra-high bypass ratio engines for an over-wing aircraft configuration. *Journal of the Global Power and Propulsion Society*, 2:493–515, 2018.
- [33] B. V. Johnson. Internal air and lubrication systems. In *Encyclopedia of Aerospace Engineering*. John Wiley & Sons, Ltd, 2010.
- [34] M. Steiner, S. Zerobin, S. Bauinger, F. Heitmeir, and E. Göttlich. Development and commissioning of a purge flow system in a two spool test facility. In *12th European Conference on Turbomachinery Fluid dynamics & Thermodynamics, Stockholm, Sweden, Apr*, pages 3–7, 2017.
- [35] A. Moore. Gas Turbine Engine Internal Air Systems: A Review of the Requirements and the Problems. volume ASME 1975 Winter Annual Meeting: GT Papers of *Turbo Expo: Power for Land, Sea, and Air*, page V001T01A001, November 1975.
- [36] M. Pau, G. Paniagua, D. Delhayé, A. de la Loma, and P. Ginibre. Aerothermal Impact of Stator-Rim Purge Flow and Rotor-Platform Film Cooling on a Transonic Turbine Stage. *Journal of Turbomachinery*, 132(2):021006, January 2010.
- [37] M. Fiore, N. Gourdain, JF. Boussuge, and E. Lippinois. Delineating Loss Sources Within a Linear Cascade With Upstream Cavity and Purge Flow. *Journal of Turbomachinery*, 141(9):091008, June 2019.
- [38] J. D. Denton. Loss Mechanisms in Turbomachines. volume Volume 2: Combustion and Fuels; Oil and Gas Applications; Cycle Innovations; Heat Transfer; Electric Power; Industrial and Cogeneration; Ceramics; Structures and Dynamics; Controls, Diagnostics and Instrumentation; IGTI Scholar Award of *Turbo Expo: Power for Land, Sea, and Air*, 05 1993. V002T14A001.
- [39] K. D. Gallier, P. B. Lawless, and S. Fleeter. Development of the Unsteady Flow on a Turbine Rotor Platform Downstream of a Rim Seal. volume Volume 5: Turbo Expo 2004, Parts A and B of *Turbo Expo: Power for Land, Sea, and Air*, pages 939–947, June 2004.
- [40] L. Schäflein, J. Janssen, H. Brandies, P. Jeschke, and S. Behre. Influence of Purge Flow Injection on the Performance of an Axial Turbine With Three-Dimensional Airfoils and Non-Axisymmetric Endwall Contouring. *Journal of Turbomachinery*, 145(6):061004, December 2022.
- [41] H. P. Hodson and R. J. Howell. Bladerow interactions, transition, and high-lift aerofoils in low-pressure turbines. *Annual Review of Fluid Mechanics*, 37(1):71–98, 2005.
- [42] N. Fard Afshar, D. Kozulovic, S. Henninger, J. Deutsch, and P. Bechlar. Turbulence anisotropy analysis at the middle section of a highly loaded 3d linear turbine cascade using large eddy simulation. *Journal of the Global Power and Propulsion Society*, 7:71–84, 2023.
- [43] A. Smirnov, S. Shi, and I. Celik. Random Flow Generation Technique for Large Eddy Simulations and Particle-Dynamics Modeling. *Journal of Fluids Engineering*, 123(2):359–371, February 2001.

- [44] M. Okada, L. Simonassi, G. Lopes, and S. Lavagnoli. PIV Measurements in a High-Speed Low-Reynolds Low-Pressure Turbine Cascade. volume Proceedings of ASME Turbo Expo 2023 of *Turbomachinery Technical Conference and Exposition*, June 2023. GT2023-102156.
- [45] G. Lopes, L. Simonassi, and S. Lavagnoli. Time-Averaged Aerodynamics of a High-Speed Low-Pressure Turbine Cascade with Cavity Purge Flow and Unsteady Wakes. volume Proceedings of ASME Turbo Expo 2023 of *Turbomachinery Technical Conference and Exposition*, June 2023. GT2023-102828.
- [46] S. Lavagnoli, G. Lopes, L. Simonassi, and A. F. M. Torre. SPLEEN - High Speed Turbine Cascade – Test Case Database, June 2023.
- [47] T. Passot and A. Pouquet. Numerical simulation of compressible homogeneous flows in the turbulent regime. *Journal of Fluid Mechanics*, 181:441 – 466, September 1987.
- [48] P. Lepage. Implémentation de la technique de simulation des grandes échelles dans un solveur parallèle de dynamique des fluides. Mémoire, Université de Sherbrooke, 2013.
- [49] A. Boudin. Turbulence injection methods for large-eddy simulations. Working note, Cerfacs - ISAE SUPAERO, 2021.
- [50] R. H. Kraichnan. Diffusion by a Random Velocity Field. *Physics of Fluids*, 13(1):22–31, January 1970.
- [51] G. R. Tabor and M. H. Baba-Ahmadi. Inlet conditions for large eddy simulation: A review. *Computers & Fluids*, 39(4):553–567, 2010.
- [52] N. Anton and W. Wiberg. *Aerodynamic design of a gas turbine rotor blade for the KTH test turbine*. Master’s thesis, Lund University, 2013. ISRN LUTMDN/TMHP–13/5284–SE.
- [53] W. Zhang, Z. Zou, and J. Ye. Leading-edge redesign of a turbomachinery blade and its effect on aerodynamic performance. *Applied Energy*, 93:655–667, 2012. (1) Green Energy; (2)Special Section from papers presented at the 2nd International Eney 2030 Conf.
- [54] M. Fiore. *Influence of cavity flow on turbine aerodynamics*. Phd thesis, Institut Supérieur de l’Aéronautique et de l’Espace, May 2019.
- [55] L. S. Langston. Secondary flows in axial turbines—a review. *Annals of the New York Academy of Sciences*, 934(1):11–26, 2001.
- [56] H. P. Wang, S. J. Olson, R. J. Goldstein, and E. R. G. Eckert. Flow Visualization in a Linear Turbine Cascade of High Performance Turbine Blades. *Journal of Turbomachinery*, 119(1):1–8, January 1997.
- [57] J. Jeong and F. Hussain. On the identification of a vortex. *Journal of Fluid Mechanics*, 285:69–94, 1995.
- [58] C. Koupper, L. Gicquel, F. Duchaine, T. Bacci, B. Facchini, A. Picchi, L. Tarchi, and G. Bonneau. Experimental and numerical calculation of turbulent timescales at the exit of an engine representative combustor simulator. *Journal of Engineering for Gas Turbines and Power-Transactions of the ASME*, 138(2):021503–021513, 2015.
- [59] A. Boudin, J. Dombard, F. Duchaine, L. Gicquel, N. Odier, S. Lavagnoli, G. Lopes, L. Simonassi, and C. Uribe. Analysis of Rotor/Stator Interactions in a High-Speed Low-Pressure Turbine Cascade Using Large-Eddy Simulations. volume Proceedings of 15th European Conference on Turbomachinery Fluid dynamics & Thermodynamics, April 2023. ETC2023-257.

- [60] M. Emory and G. Iaccarino. Visualizing turbulence anisotropy in the spatial domain with componentality contours. *Center for Turbulence Research Annual Research Briefs*, pages 123–138, 2014.
- [61] J. L. Lumley and G. R. Newman. The return to isotropy of homogeneous turbulence. *Journal of Fluid Mechanics*, 82(1):161–178, 1977.
- [62] S. Banerjee, R. Krahl, F. Durst, and Ch. Zenger. Presentation of anisotropy properties of turbulence, invariants versus eigenvalue approaches. *Journal of Turbulence*, 8:N32, 2007.
- [63] C. Bailly, X. Gloerfelt, and C. Bogey. Report on stochastic noise source modelling. May 2002.
- [64] N. Guézennec. *Contrôle actif de la combustion diphasique*. Phd thesis, Institut National Polytechnique de Toulouse, March 2010.